ANALYSIS OF ADDITIVELY MANUFACTURED LATTICE STRUCTURES BY FINITE ELEMENT METHODS

THESIS

Christopher A. Box, Captain, USAF

AFIT-ENY-MS-17-M-245

DEPARTMENT OF THE AIR FORCE
AIR UNIVERSITY

AIR FORCE INSTITUTE OF TECHNOLOGY

Wright-Patterson Air Force Base, Ohio

AFIT-ENY-MS-17-M-245

ANALYSIS OF ADDITIVELY MANUFACTURED LATTICE STRUCTURES BY FINITE ELEMENT METHODS

THESIS

Presented to the Faculty

Department of Astronautical Engineering

Graduate School of Engineering and Management

Air Force Institute of Technology

Air University

Air Education and Training Command

in Partial Fulfillment of the Requirements for the

Degree of Master of Science in Astronautical Engineering

Christopher A. Box, B.S.M.E.

Captain, USAF

March 3, 2017

AFIT-ENY-MS-17-M-245

ANALYSIS OF ADDITIVELY MANUFACTURED LATTICE STRUCTURES BY FINITE ELEMENT METHODS

Christopher A. Box, B.S.M.E.
Captain, USAF

Committee Membership:

Major Ryan O'Hara, PhD
Chair

Dr. Anthony Palazotto, PhD
Member

Dr. Eric Swenson, PhD
Member

AFIT-ENY-MS-17-M-245

Abstract

Additive Manufacturing (AM) processes are well known for their ability to fabricate parts with complex geometries. Lattice structures leverage this ability to create parts with high strength-to-weight ratio and other desirable structural qualities. This research presents a parameterized modeling tool using common Finite Element Analysis (FEA) and scripting software with which aggregated lattice structures can be analyzed, given different geometric properties and loading conditions. A full factorial Design of Experiments is run to explore the effects of various parameters on the strength of lattice structures. Experimental compressive strength results from three Fused Deposition Modeling (FDM)-produced Polylactic Acid (PLA) lattices are discussed and compared to predictions from the Finite Element simulations.

Acknowledgments

I would like to thank my advisor, Maj O'Hara, for the effort and mentorship provided to me throughout the course of this research. You kept me on track in countless weekly meetings. I would like to thank Dr. Philip Flater of AFRL for the collaboration and advice received throughout this endeavor. I'd like to extend my thanks to Matt Lippert and Travis Shelton, whose printer maintenance and printing assistance was invaluable to completion of my work. Thanks goes out to my committee members, Dr. Palazotto and Dr. Swenson, for taking the time to provide feedback on my writing. I'd also like to thank my friends, family, and classmates for withstanding the repeated use of the phrases "working on my thesis" and "crush some lattices." Finally, I'd like to dedicate this paper to my mom, whose love and support for me and my academic (and all other) endeavors was always unwavering.

Christopher A. Box

Table of Contents

Page

List of Figures

Figure Page

List of Tables

List of Acronyms

ABS Acrylonitrile Butadiene Styrene

AM additive manufacturing

APDL ANSYS Parametric Design Language

BCC Body-Centered Cubic

DOE Design of Experiments

DOF Degrees of Freedom

EBM Electron Beam Melting

FCC Face-Centered Cubic

FDM Fused Deposition Modeling

FE Finite Element

FEA Finite Element Analysis

FEM Finite Element Model

PLA Polylactic Acid

SLA Stereolithography

SLM Selective Laser Melting

List of Symbols

$[K]$	Global Stiffness Matrix
$\{D\}$	Displacement vector
$\{R\}$	Load vector
δ	Displacement
$\propto$	is proportional to
ρ_s	Solid Material Density
ρ_{rel}	Relative Density
σ_y	Solid Material Yield Strength
σ_{pl}	Lattice Plateau Strength
θ	Auxetic Re-entrant Strut Angle
$\tilde{\rho}$	Lattice Density
$\tilde{E}$	Lattice Elastic Modulus
A	Cross Sectional Area
b	number of struts for Maxwell's Stability Criterion
b_{new}	y-intercept of 0.2% offset line
b_{old}	y-intercept of linear force-displacement data
c_s	Cell Size
d	Strut Solid Diameter
E_s	Solid Material Elastic Modulus
E_{rel}	Relative Elastic Modulus
F	Force
H	Lattice Overall Height
h	Height of Auxetic Vertical Strut
j	number of joints for Maxwell's Stability Criterion
K	Lattice Stiffness
k_i	Number of Levels for i'th factor
L	Length of Material Block
l_i	Length of i'th Strut
L_s	Strut length
L_{aux}	Length of Auxetic Re-entrant Strut
L_{eff}	Effective strut length
M	Maxwell's Stability Criterion
m	Lattice Mass
n_x	Number of cells in x direction
n_y	Number of cells in y direction
n_z	Number of cells in z direction
N_{cells}	Number of Cells
N_{div}	Number of Elements per Strut
N_{elem}	Number of Elements
N_{factor}	Number of Factors
N_{kp}	Number of Keypoints
N_{runs}	Number of Full Factorial Runs
N_{strut}	Number of Struts
P	Force
V_{aux}	Volume of Auxetic Unit Cell
V_{BCC}	Volume of BCC Unit Cell
V_{box}	Volume of Unit Cell bounding box
V_{cell}	Volume of Unit Cell
V_{oct}	Volume of Octet Unit Cell

ANALYSIS OF ADDITIVELY MANUFACTURED LATTICE STRUCTURES BY FINITE ELEMENT METHODS

I. Introduction

1.1 Chapter Overview

Cellular structures are the building blocks of life. Cellular structures can be seen in bones, trees, and other organic architectures as an intelligent way to minimize weight while maintaining necessary strength. Man-made, periodic cellular structures commonly referred to as lattice structures can be just as useful. Numerous examples of lattice frameworks can be seen in bridges, towers, and other large structures such as the Eiffel Tower. On a smaller scale, lattices are becoming more prevalent in aerospace, automotive, and biomedical applications [4]. These structures have many useful properties, such as high strength to weight ratio, good thermal transfer opportunities, and good energy absorption [4].

Interest in lattice structures has blossomed with the refinement of additive manufacturing (AM) techniques capable of producing more intricate designs. Additive manufacturing processes use a layer-by-layer assembly process that allows designers the ability to create complex designs that would be impossible to produce through conventional subtractive manufacturing processes. Vast improvements in technology have welcomed a corresponding improvement in this design freedom. This paper will explore and refine complex designs known as lattice structures meant for assembly using AM.

This chapter will provide an overview of the research objectives, motivation, rel-

evant background information, and methodology used to accomplish the research.

1.2 Objective

This research is meant to gain a better understanding of lattice structures, their structural properties, and their manufacturability using the Fused Deposition Modeling (FDM) AM process. The following main objectives were developed to accomplish these goals:

- Develop a parametric modeling tool for lattice structures using Finite Element Analysis (FEA)
- Characterize the effects of critical design parameters on the performance of lattice structures under compression loading
- Correlate predicted unit cell behavior to experimental compression of additively manufactured lattice structures

1.3 Motivation

A simple to use Finite Element Model (FEM) for lattice structures is useful to predict the behavior of a lattice structure without using the time and resources to test samples experimentally. A parameterized tool for analyzing unit cells with different geometrical properties for given initial conditions will help engineers and designers choose an appropriately strong lattice for their purposes. Some commercial software programs today such as nTopology and Altair Optistruct use their own built-in Finite Element (FE) tool for lattice manipulation, but are typically proprietary. Using a mature FEA program such as ANSYS allows the user to export results and lends more transparency to the process. Additionally, a dedicated FE software program will have more analysis options. The need for an accurate and validated tool for rapid

creation and analysis of additively manufactured lattice structures is the primary motivation for this effort. This need ties directly to a main objective, the creation and validation of a tool to model, analyze, and iterate lattice structures using a mature FEA program.

1.4 Background

Lattice structures are also commonly referred to as "periodic cellular structures", as they completely fill a 3D space with a repeating geometry. The smallest geometric entity that can uniformly repeat and fill a volume without gaps is referred to as the unit cell. Unit cells come in various shapes, including cubic, hexahedral, tetrahedral, and hexagonal. Others are defined by functional surfaces. Lattice structures are commonly used as internal support in parts, decreasing weight while maintaining a required stiffness. They have also been used for vibration dampening and thermal transfer. Various methods of assembly have been used to manufacture lattice structures and will be discussed more in Chapter 2. AM processes have broadened the interest in lattice structures, due to their ease of manufacturability and ability to make more complex designs.

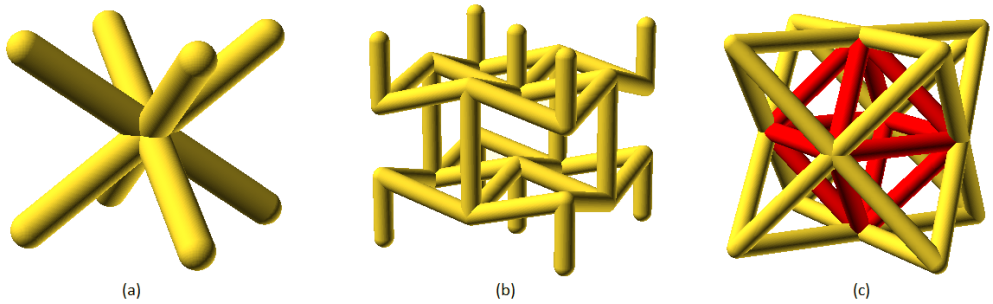

Figure 1.1. Three unit cell geometries studied in this research. (a) "Body Centered Cubic [BCC]" or "Vertex Centroid" (b) Auxetic "Re-entrant" (c) "Octet truss" (internal struts highlighted red for clarity)

1.5 Assumptions

Certain key assumptions were made in this research. A linear FEM approach was utilized. Struts were modeled as beam elements, which have no physical volume. Rather, they mathematically represent cross section properties on a 1 dimensional line through 3 dimensional space. Joints at strut intersections are considered rigid, as opposed to pin jointed or other connection methods. 3D printed material is assumed to be isotropic. This is not true, but for the most part effects will be small since testing will take place in the build direction. Only cubic unit cells were examined in this study. This was done in order to reuse the same code for three different unit cell geometries. The auxetic re-entrant unit cell can be defined with a different length in each dimension, however a non-cubic rectangular prism aggregation scheme would require cell-specific code that would complicate the full factorial Design of Experiments (DOE) setup for the other two cells. Other shapes were considered and can be examined in the future.

1.6 Methodology

The first step in accomplishing the research objectives was development of a tool to write and execute a FEA script for three different lattice structure geometries, which are shown in Figure 1.1. The coding process and design choices made will be discussed in Chapter 3. The abilities to define a parameterized geometry and iteratively perform FEA are key attributes that will also be reviewed.

A full factorial DOE study varied key parameters for each lattice topology to find the top performing lattices in a compression loading scenario. Results from this study show strength trends for unit cell type, relative density, and strut shape. Several other smaller studies examined additional areas of interest, such as the effects of keypoint offset error, strut deletion percentage, and auxetic re-entrant cell strut angle, which

will be explained in the next two chapters.

Finally, selected top performing lattices were printed via FDM and were compression tested for comparison with the finite element model. Results of the experimental tests and the FEM are discussed, along with areas for improvement and future work.

1.7 Thesis Overview

- Chapter I: States the objective of this thesis, establishes the motivation, and briefly discusses the background and methodology
- Chapter II: Discusses the theory presented in relevant literature related to lattice structural properties, additive manufacturing, and finite element modeling
- Chapter III: Lists modeling and testing methodology used for this research
- Chapter IV: Presents and discusses the results of FEA and experimental testing
- Chapter V: Summarizes the results, draws conclusions, and discusses recommendations for future research

II. Background

2.1 Chapter Overview

This chapter will discuss the current state of research in cellular lattice structures and additive manufacturing (AM) technology. An extensive literature search was performed to examine current trends and areas of examination of additively manufactured lattice structures. Relevant findings are presented in this chapter.

2.2 Cellular and Lattice Structures

2.2.1 Background

Cellular solid materials consist of foams, meshes, and lattices. Many cellular materials like foams are stochastic, meaning without order. Lattices are a structured type of cellular material with an intentional, repetitious geometry. Cellular materials are known for their unique properties including stiffness, strength, thermal conductivity and diffusivity, energy absorption, and electrical resistivity. These materials can be open or closed cell; stochastic or ordered; ceramic, polymer, or metal. Ashby [1] gives three underlying principles that affect cellular material properties:

1. The properties of the solid material
2. The topology (connectivity) and shape of the cell edges and faces
3. The relative density ρ_{rel} of the foam

He describes the relative density of the foam as the ratio of the foam density to the foam material's solid density. Relative density can also be considered the volume fraction.

Cellular lattice structures have long been studied as a way to maximize strength while minimizing weight. In 1903, Alexander Graham Bell studied a repeating, 3-dimensional tetrahedral shape used as lightweight structural support members in kites, as part of a larger effort to create a flying machine [5]. Since then, numerous unit cell geometries that completely fill a 3D volume have been devised and studied [6, 7] . Common cell types include tetrahedral, octahedral, hexahedral (including cubic), and honeycomb.

2.2.2 Parameters and Definitions

Unit cell geometries are usually defined by "keypoints" and "struts". Keypoints refer to a collection of points in 3D space, and struts refer to a collection of lines each connecting two keypoints. Keypoints typically define the intersection of two or more struts. (The term node is also commonly applied to points where struts intersect. To prevent confusion with Finite Element Analysis (FEA) terminology later, points defining strut connectivity will be called "keypoints". "Nodes" will be used later to define additional points along a strut.) A thickness can be applied to lines to represent a volume, either physically or mathematically. However, not all unit cells are defined by points and lines. Tessellated geometries (those that fill space entirely without overlap) have also been made using infinitely periodic functional surfaces, like the Schoen Gyroid [6]. Its surface geometry is defined by a three dimensional trigonometric function.

Unit cells have many parameters that can be modified to produce different geometries. As previously mentioned, a variety of unit cell shapes can be chosen to fill a given volume. Within a given unit cell shape, number of struts and arrangement of struts can be modified. Consider a simple cubic unit cell with 9 keypoints, one at each corner and one at the centroid of the cube. Several different geometries can be

realized by changing the connected keypoints. Eight lines, each a connection from a corner to the center is a basic Body-Centered Cubic (BCC) unit cell (Figure 2.4 or 1.1a). Adding the vertical edge struts gives a variant called BCCZ. Solely using the edge connections gives a simple box unit cell. Some organizations have developed unit cell databases to organize and store different shapes [7].

Three other related parameters are the unit cell size, strut diameter, and relative density. By thickening the struts, the relative density will increase. Increasing the unit cell size while maintaining a constant strut diameter will decrease the relative density. Several sources indicate that cell density has one of the strongest correlations to overall lattice strength [1].

2.3 Bending vs. Stretching Dominated Structures

Ashby characterizes cellular structures into three types: bending-dominated, stretching-dominated, and over-constrained [1]. Figure 2.1 shows examples of each. A large majority of foams and lattice structures are considered bending-dominated, which means their primary failure mechanism is the bending of the struts. In a stretch-dominated lattice, the struts under loading carry tension or compression. Slender structures, due to their low second moment of area, are much stiffer in tension or compression than in bending, and therefore stretch-dominated structures are more efficient load bearers in tension or compression. A third type is over-constrained, which has some degree of self-stress even in an unloaded state due its strut connectivity. However, struts are again mostly in tension or compression and therefore over-constrained cells can be considered stretch-dominated. Maxwell's Stability Criterion can be used to determine which of these three types a structure is.

$$M = b - 3j + 6 \tag{2.1}$$

Where

M = Maxwell's Stability Criterion

b = number of struts

j = number of joints (keypoints)

Eq. 2.1 is Maxwell's Stability Criterion for three dimensions. If M $<$ 0, the lattice is bending dominated. If M $>=$ 0, the lattice is stretch-dominated, and designated "over-constrained" if M $>$ 0.

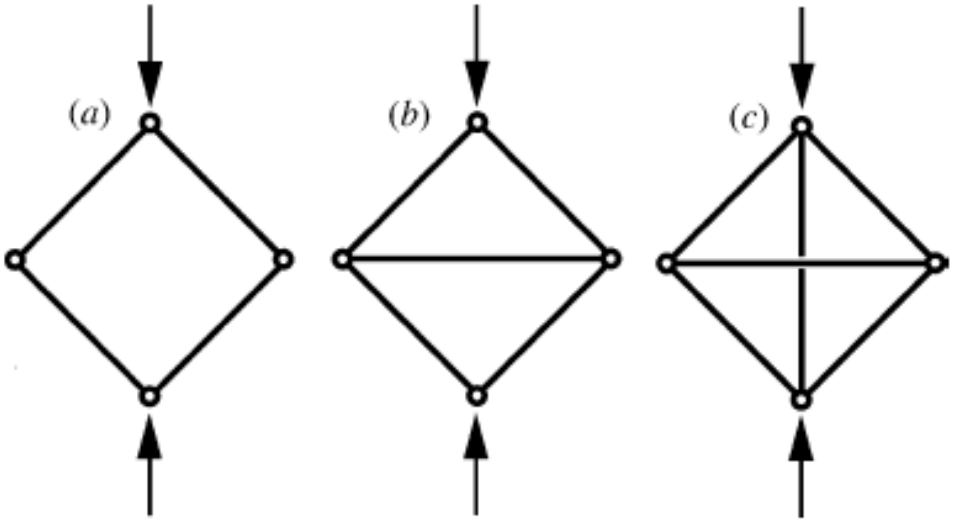

Figure 2.1. 2D examples of the three lattice classifications: (a) Bending-dominated, (b) Stretching-dominated, and (c) Over-constrained. [1]

Ashby [1] presents several scaling laws to describe lattice mechanical properties. Equation 2.2 shows the relationship between relative elastic modulus and relative density for bending-dominated structures. Equation 2.3 shows the relative strength to relative density relationship for plastic strut failure of bending-dominated structures. For stretching-dominated structures, Equation 2.4 shows the modulus to density relationship, and Equation 2.5 shows the strength to density relationship for plastic strut failure. This study focuses on the elastic modulus and stiffness of the lattice structures and will utilize equations 2.2 and 2.4.

$$\frac{\tilde{E}}{E_s} \approx \left(\frac{\tilde{\rho}}{\rho_s}\right)^2 \tag{2.2}$$

Where

$\frac{\tilde{E}}{E_s} = E_{rel}$ = Relative elastic modulus

$\frac{\tilde{\rho}}{\rho_s} = \rho_{rel}$ = Relative density

$\tilde{E}$ = Elastic modulus of lattice

E_s = Elastic modulus of solid material

$$\frac{\sigma_{pl}}{\sigma_y} \approx 0.3\left(\frac{\tilde{\rho}}{\rho_s}\right)^{1.5} \tag{2.3}$$

Where

$\frac{\sigma_{pl}}{\sigma_y} = \sigma_{rel}$ = relative strength

σ_{pl} = plateau stress of lattice (Fig. 2.2)

σ_y = yield strength of solid material

$$\frac{\tilde{E}}{E_s} \approx \frac{1}{3}\left(\frac{\tilde{\rho}}{\rho_s}\right) \tag{2.4}$$

$$\frac{\sigma_{pl}}{\sigma_y} \approx \frac{1}{3}\left(\frac{\tilde{\rho}}{\rho_s}\right) \tag{2.5}$$

Examined in Ashby's study is how the relative elastic modulus E_{rel} of a stretching-dominated structure scales linearly with ρ_{rel}, whereas E_{rel} of a bending dominated structure scales with ${\rho_{rel}}^2$. These two relations show that for a given ρ_{rel} between 0 and 1, stretching dominated structures are stiffer. However, he adds that stretch-dominated structures can still fail by buckling in which case $E_{rel} \propto {\rho_{rel}}^2$. If this does occur, it is usually at low relative densities. Ashby claims that for metallic foams with $\rho_{rel} < 0.01$, struts will buckle in a stretch-dominated structure [1]. In one study, a 2.4% relative density titanium lattice with stretch-dominated struts failed by buckling

[8].

It should be noted that Equations 2.2 to 2.5 were derived by treating the cellular structure as its own material with its own set of material properties, rather than a collection of individual struts, to determine overall strength and stiffness. Experimentally, there is evidence supporting that these scaling laws describe lattices structures in the millimeter scale [9].

Calculation of the relative values (E_{rel}, σ_{rel} and ρ_{rel}) assumes the same bounding volume and cross sectional area for both the lattice structure and solid material. In reality, the lattice has a smaller cross sectional area and material volume. Since the area and volume are both smaller than a solid block would be, the expectation is that force to cause yield and the structure's stiffness are both fractions of the solid block values. Therefore, the values E_{rel}, σ_{rel}, and ρ_{rel} are also fractions. This "constant dimensions" method applies to the difference between any other lattice and solid values, whether it be yield stress, strain, density, etc.

Ashby concludes that for structural applications, stretch-dominated structures are most efficient and therefore the best choice. Generalized stress-strain curves for both stretching- and bending-dominated types are shown in Figure 2.2. He notes that bending-dominated structures are better for energy absorption applications due to their long, flat plateau stress after yield. Stretch-dominated structures show significant post-yield softening, making them less effective at energy absorption. Yield stress is higher for stretch-dominated lattices, due to high strut connectivity. The eventual yielding modes consist of either plastic buckling or brittle fracture, which significantly lower the strength of the lattice post-yield. Continued compression leads to densification, where struts are deformed so much that they come in contact with one another. Stress rises abruptly at this point [1].

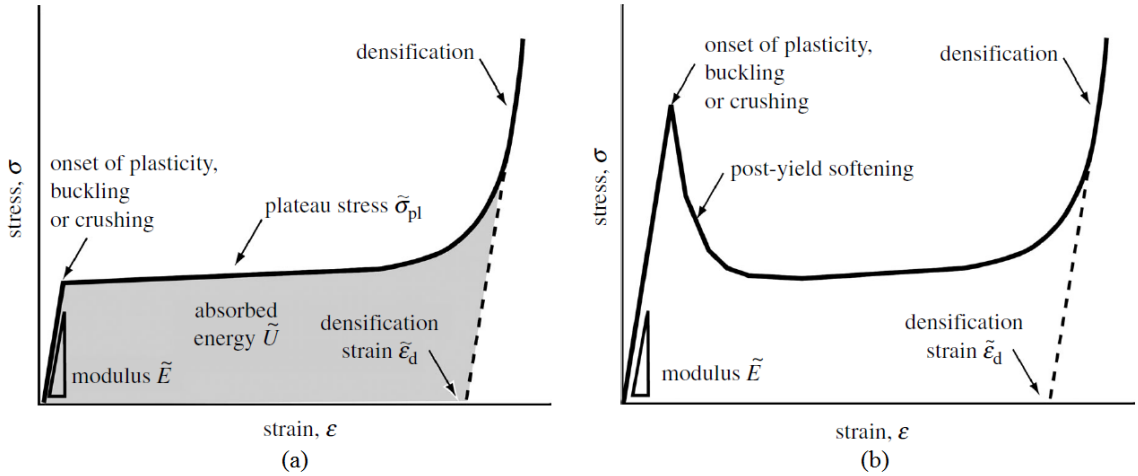

Figure 2.2. General stress-Strain curves for (a) bending and (b) stretching-dominated structures in compression [1].

Many lattice geometries are open cell structures, including the three in this study. Many open cell structures behave similarly to stochastic (randomly arranged) materials under compression which tend to be bending dominated. Conversely, lattices that behave similarly to closed cell materials under compression tend to be stretching-dominated. However, Equation 2.1 should be used to determine which behavior a lattice follows.

2.4 Cells to be Studied

This section will describe the three unit cell geometries selected for this study. Properties are listed in Table 2.1.

Table 2.1. Unit cell properties

Unit Cell	Keypoints	Struts	Cell Shape	M	Response
Body Centered Cubic	9	8	cubic	-13	Bending
Auxetic Re-entrant	28	38	hexahedral	-10	Bending
Octet-truss	14	36	cubic	0	Stretching

A generalized right-hand coordinate system is used when describing the cells and can be seen in Figure 2.3. All three dimensions x, y, and z are normal to one of

the cubic cell's three parallel pairs of faces. The most important dimension is the z dimension and is most critical to the auxetic cell because it is not fully symmetric. It is defined as the direction parallel to the "vertical" struts of length h. The z direction is the dimension in which loads are applied in the model, the build direction during fabrication, and the crush direction during compression tests. Terms such as "top", "bottom", "vertical", all refer to the z direction. "Horizontal" therefore refers to the x-y plane and is parallel to the ground or build plate on the 3D printer.

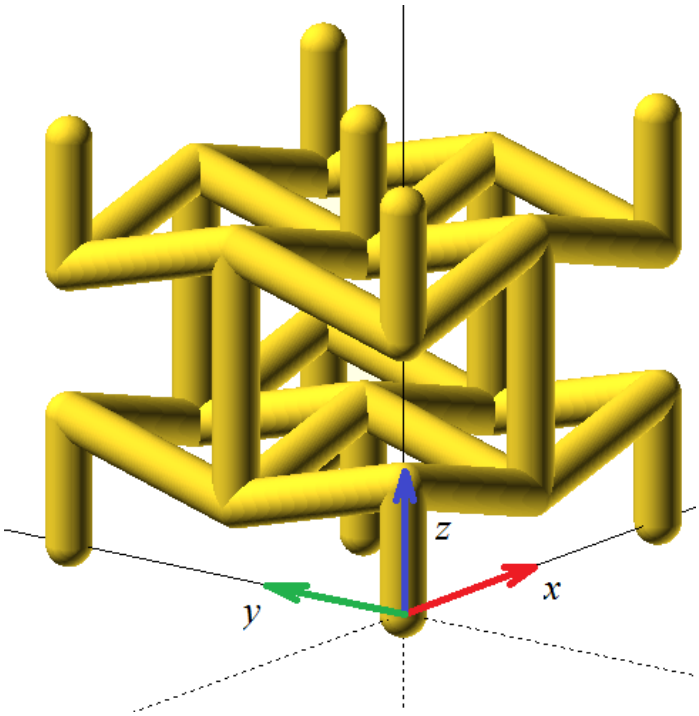

Figure 2.3. Coordinate system shown with the Auxetic re-entrant unit cell.

2.4.1 Body Centered Cubic (BCC) Cell

The Body Centered Cubic unit cell is a common, straightforward lattice unit cell. Other names for it include octahedral or vertex centroid (nTopology). Per Maxwell's Stability Criterion (Eq. 2.1), it is a bending dominated structure. Its shares a name with the atomic packing arrangement because of its similar keypoint arrangement. As mentioned previously, it has 9 keypoints and 8 struts, with each strut connecting

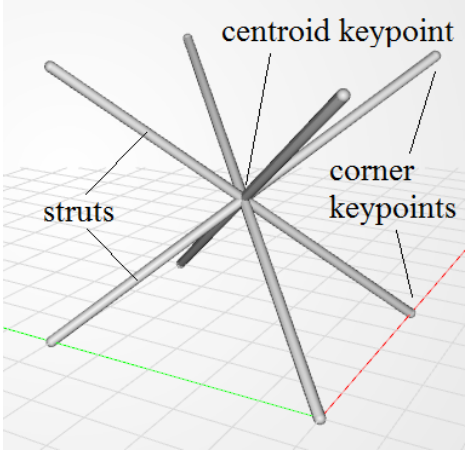

Figure 2.4. The Body Centered Cubic (BCC) unit cell.

a corner keypoint to the centroid keypoint. Its relative density is relatively low compared to other cells with the same strut diameter. The BCC cell has the unique characteristic of fully containing all of its struts within the cubic cell boundary and not sharing struts with adjoining cells. It does though share its eight outer keypoints.

2.4.2 Auxetic Re-entrant Cell

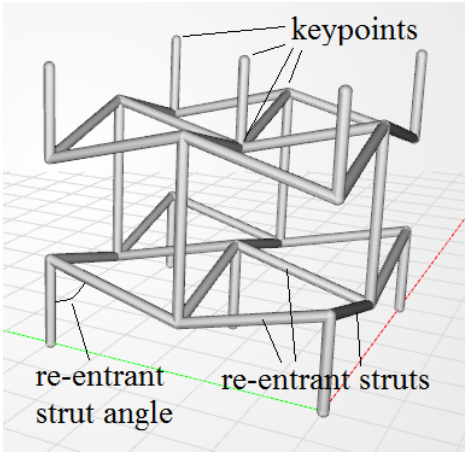

Figure 2.5. Auxetic re-entrant unit cell.

Auxetic materials exhibit unique properties where they densify under compression and expand under tension which is quantified by a negative Poisson's Ratio. Poisson's ratio reflects the amount of transverse expansion experienced when subjected to axial

compression (or contraction when in tension). For most ordinary materials, Poisson's ratio is a positive number because a change in one dimension produces the opposite change in the others [10, 11].

The auxetic re-entrant cell (or auxetic re-entrant honeycomb) is a 3D structure that has auxetic properties. Its behavior is considered anisotropic because displacement in the loading and lateral directions is different [12]. Of the three cells in this study, it is the only one not fully symmetric in all three axes; however, it symmetric about x and y. A single unit cell is comprised of 26 keypoints and 38 struts. It shares struts with the eight neighboring cells in the x-y plane and connects directly to two others above and below.

The auxetic geometry is shown in Figure 2.6. Two of the three variables are required to fully define the cell. In general, the bounding cell shape is a rectangular prism. Given appropriate values for the re-entrant strut length L_{aux}, vertical strut length h, and re-entrant strut angle θ, the cell can be cubic, as it is in this study.

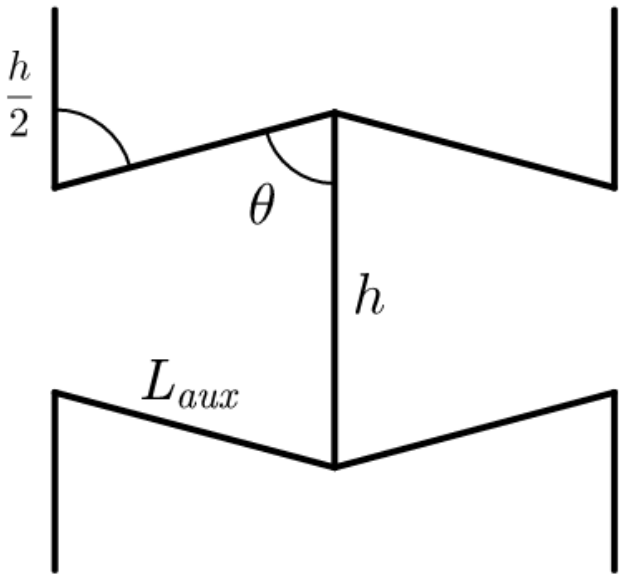

Figure 2.6. Outermost struts of Auxetic re-entrant unit cell, showing geometry-defining parameters.

2.4.3 Octet-truss

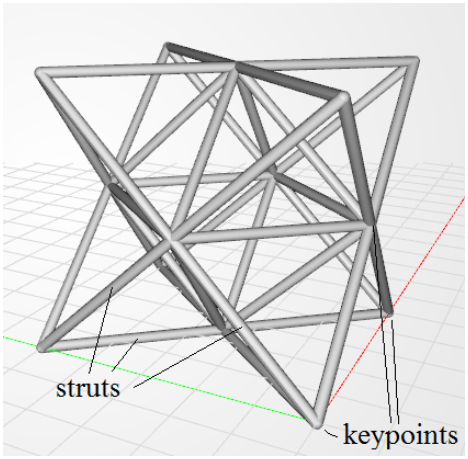

Figure 2.7. The Octet-truss unit cell.

Octet-truss unit cells are some of the most efficient load carriers per weight and have been suggested for use in structural applications [13, 14]. The cell is stretch-dominated, loading each strut primarily in either tension or compression. They are occasionally referred to as Face-Centered Cubic (FCC) cells, again an atomic arrangement reference. They have a higher relative density than the previous two cells for a given strut diameter. A single cell has 14 keypoints and 36 struts, with all of the outer struts shared with adjacent cells.

2.5 Additive Manufacturing

2.5.1 History and Background

Additive manufacturing has roots back in the late 1800s, in the areas of photo sculpture and topography [15]. These two technologies evolved into photo-glyph recording, selective exposure of light-sensitive polymers, in the 1950s. A method very similar to photo-glyph recording, Stereolithography (SLA) was patented and commercialized in the mid 1980s. It wasn't until then that AM became a plausible method of production. Since then, technology has taken massive leaps forward in terms of

capability and accessibility. Four general methods of AM have been developed: vat photopolymerization (e.g. SLA), powder bed fusion (e.g. Selective Laser Melting (SLM)), material extrusion, and binder jetting [15].

Of these four categories, material extrusion is most widely known. It is associated with the "Maker Movement", a surge in do-it-yourself home use AM machines and software that allow individuals the capability to design and create parts. These printers are most commonly material extrusion/Fused Deposition Modeling (FDM) technology, which deposits thin polymer layers of a part through use of a translating nozzle. Plastics like Polylactic Acid (PLA) and Acrylonitrile Butadiene Styrene (ABS) are usually the materials of choice for these printers and are very capable of producing low to medium quality parts. PLA is used in this study.

Though plastic printers are useful for lightweight prototypes, the material properties limit their use in high strength applications. Some material extrusion techniques have attempted use of metal pastes and metal-infused filaments, but powder bed fusion is still the primary method for additively manufacturing metal components [15]. Selective Laser Melting (SLM) and Electron Beam Melting (EBM) are the two most common types of powder bed fusion. Both processes use directed energy to melt an atomized powder bed. SLM uses a laser while EBM uses a beam of electrons. Stainless steel, titanium, and aluminum powders have all been used. Inert gas flows into the build chamber so that highly flammable powders like aluminum and titanium cannot combust.

AM technology as a whole has improved drastically over the past decade. While AM originally was and still is used to manufacture prototype parts, the increase in precision of new AM machines has allowed some companies to manufacture production parts, such as General Electric's turbine engine fuel nozzle. SLM-produced parts are rapidly assimilating into automotive, aerospace, and medical applications. The

advantages AM processes provide over conventional subtractive methods include:

- Increased flexibility of design and design changes
- Increased geometric complexity
- Feasibility of low quantity or unique part production
- Reduced or simplified assembly
- Reduced logistics footprint

Most 3D printers read .STL files to generate parts [16]. The acronym STL originated with Chuck Hull and the SLA process, but more recently additional names have been adopted such as "standard tesselation language" and "stereolithography triangle language." In this format, a 3D object is broken into triangular surface elements defined by their three vertices and an outward normal vector. This defines the part as a hollow shell with no thickness. Either proprietary or third party slicing software uses the shell to define each individual layer of the part to be built. The printer generates build paths from the layer data and then constructs the part [16].

2.5.2 Manufacturing of Lattices

Many researchers have examined the mechanical properties of lattice structures. Rashad et al. [4] gives an overview of different manufacturing processes and summarizes the findings of several articles.

Previous studies have manufactured metal lattice structures through a variety of conventional manufacturing methods as well as a variety of additive methods using a variety of materials [4]. Conventional methods include investment casting [13], deformation forming [17], brazed snap-together assembly [8], and brazed woven and non-woven metal textiles [18]. Different approaches produce lattices with different

methods of failure and mechanical properties. Some of these methods have a limited design space, the non-woven textile approach being one example. In this method, lattices are constructed using straight metal wires stacked across each other and brazing them together. Arrangements of straight wires limit the geometry of the unit cell produced. Woven metal textiles improve on this limitation by bending the wires, but still fundamentally has a narrow design space.

Some conventional manufacturing techniques can be time consuming and waste more material when compared to SLM. This is especially true for investment casting, which builds a sacrificial polymer or wax truss (often by material deposition AM). The truss is coated with ceramic slurry which hardens to produce a mold, which can later be used to form molten metal into lattices. The sacrificial wax used to create the mold and is later removed and discarded.

2.5.3 Applicable Research

In this section, studies involving lattices and foams produced by additive and non-additive methods are discussed.

Ushijima et al.[19] analyzed the compressive properties of stainless steel BCC cells. Equations for calculating the initial stiffness (elastic modulus) and plastic collapse strength (yield strength) are presented and compared to experimental results and FEA predictions that used both beam and solid elements. It was found that when the ratio of strut diameter to cell size is relatively small ($d/L < 0.1$), the experiments and predictions are in agreement. Above this ratio, the predictions tend to underestimate the actual results [19].

Deshpande [13] reviews the octet-truss structure analytically and through Finite Element Model (FEM), then compared to experimental data gathered from an LM25 aluminum alloy octet-truss. Good agreement is seen between all three. Stiffness

is lower than predicted due to "bedding-in" effects at nodal regions. However, the stiffness and strength values seen are approximately half of the theoretical maximum values for an isotropic voided material. Strength values are shown between 3-10 times higher than a typical metallic foam. The authors forsee uses as strong, lightweight, and possibly multifunctional structural materials.

Dong et al.[8] manufactured Titanium (Ti6Al4V) octet-truss lattice structures via a snap-fit and vacuum brazing that showed excellent mechanical properties. Cell relative densities ranged from 2 to 16%. At some relative density value between 0.024 and 0.046, the initial failure mode changed from elastic buckling to inelastic buckling. Samples with relative density of 0.046 and higher all experienced permanent deformation at first failure.

Andrews et al.[20] looked at metallic foams to determine the minimum number of cells needed to neglect edge effects. Stress concentrations in cells near structure edges can affect the overall performance of a structure if the structure relies on many edge cells that are not supported by adjacent cells. Experimental tests were done on open and closed cell aluminum foams to find convergence on the elastic modulus and collapse strength. Results indicated that 6 cells in the x and y dimensions for a z-dimension compressive load were adequate to find the elastic modulus. Above eight and five cells, for open and closed cell geometries, respectively, showed convergence of the collapse strength. For auxetic cells with negative Poisson's Ratios near -1, Lakes [21] predicts a low dependence on number of cells, which is demonstrated by Yang et al.[2].

Reviews of auxetic foams for AM demonstrated enhanced properties including mechanical hardness, toughness, stiffness and dampening. Cell geometry is said to be the primary factor in determining the mechanical properties [12].

Yang et al.[2] analyzed, modeled, and tested Titanium (Ti6Al4V) auxetic re-

entrant honeycomb structures to determine their mechanical properties and Poisson's ratios. Equations in terms of the geometric parameters were derived to give elastic modulus and strength predictions. Samples were manufactured using EBM. Parameters used are shown in Table 2.2. For samples A1 and A2, a cube of 4 unit cells per dimension (4x4x4) was used and a 4x4x3 was used for the others. The 45 degree strut angles gave the most negative Poisson's Ratio, meaning they were best at condensing. The FEA results and experimental data were generally in good agreement of

Table 2.2. Design parameters for compression in the z direction. From Yang et al.[2].

Design	θ (deg)	h (mm)	L (mm)	h/L	t (mm)	Relative density (%)	ν_{zx}
A1	70	5.50	4.26	1.29	0.8	12.77	-0.37
A2	70	4.13	3.19	1.29	0.8	19.96	-0.37
A3	45	7.74	3.78	2.05	0.8	23.30	-1.90
A4	45	6.46	3.15	2.05	0.8	31.09	-1.90

each other, usually within one standard deviation of the experimental data. Analytical predictions on the other hand either under- or over-estimated the experimental data. Major conclusions drawn were that the "characteristic strut ratio" h/L and re-entrant angle θ both have significant effects on the mechanical properties and that 3 or more auxetic cells per dimension is adequate to neglect edge effects. Results from the edge effect study can be seen in Figures 2.8 and 2.9.

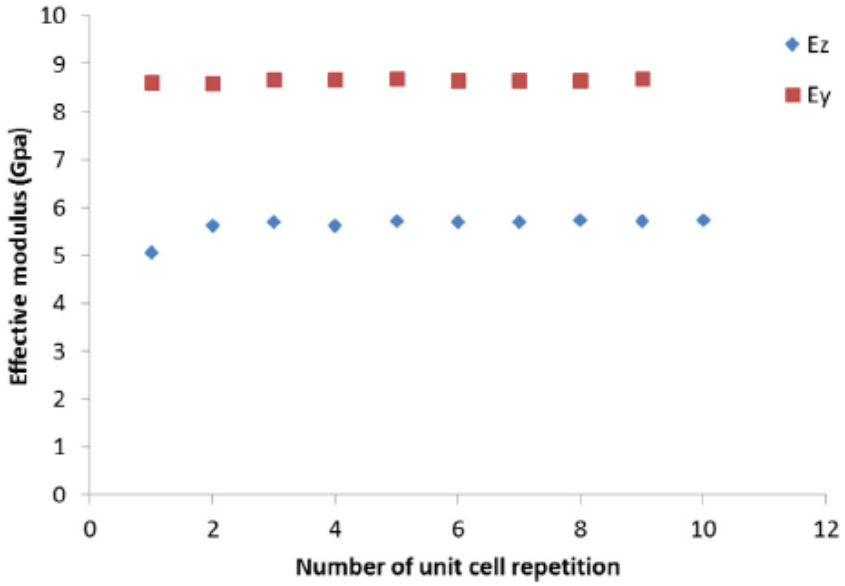

Figure 2.8. Size effect elastic modulus convergence, from Yang et al.[2].

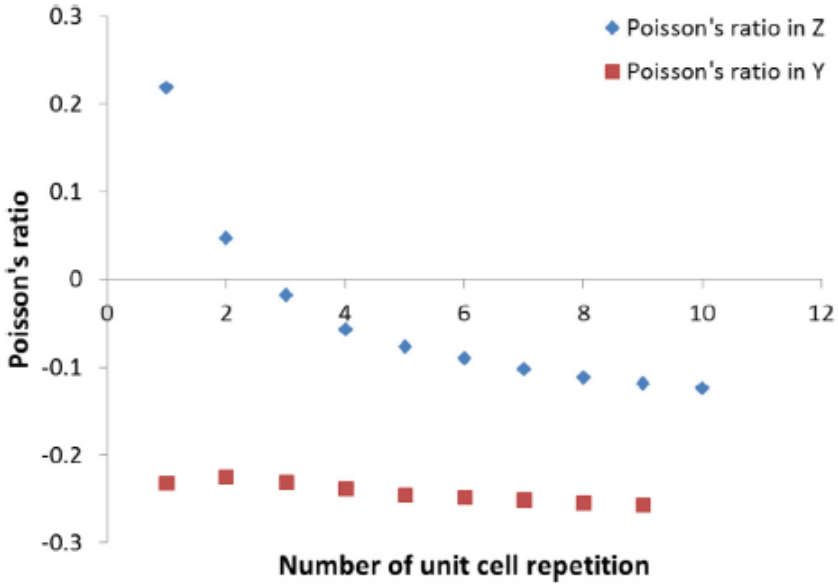

Figure 2.9. Size effect poisson's ratio convergence, from Yang et al.[2].

2.5.4 Anisotropy

It has been well documented that components made via AM have anisotropic material properties [22, 23, 24]. The effect of build angle on material properties has been studied by several researchers, but no clear conclusion has emerged. Meier and Haberland [25] performed tensile tests on SLM-produced specimens with longitudinal axes built at 0°, 45°, and 90° from the build plate. These were made from stainless steel powder (316L, X2 CrNiMo 17 13 2). Their data showed that the 0° horizontal specimen had the highest strength, and strength decreased linearly as angle increased to 90° (vertical specimen). Contrary to those findings, Shifeng et al. [26] performed a similar experiment with build angles of 0, 45, 60, 75, and 90 degrees. They discovered that the specimens built off of the build plate (45° and higher) exhibited much higher tensile strengths than specimens they built flat on the plate, with 45 degrees being the highest. A third source however found that a 45° angle had the worst strength of three specimens among 0, 45, and 90 degree orientations [27].

Shifeng et al. [26] theorize that the number of track-track melt pool boundaries (boundaries between two successive laser paths) determines the strength. They note that cracks propagate from these intersections, and vertical samples have fewer of these locations per cross sectional area. Fewer boundaries means smaller probability of cracking, and fewer cracks means higher strength. This theory however cannot be consistently applied to all three studies, indicating other factors also influence strength. Due to the conflicting data, this study will use the simplifying assumption that the printed material has isotropic properties to analyze the overall lattice response.

2.6 Finite Element Analysis (FEA)

FEA is a numerical analysis method that breaks a large problem down into many smaller ones. Formally, FEA allows one to calculate the spatial distribution of a continuous field. A common example of a spatially distributed field is the stress within a loaded structural member or the temperature or magnetic field distributions through space or material. FEA determines values for the continuous distribution at discrete points within the medium by breaking medium into many smaller finite pieces. The individual reaction of each piece can be solved for with given boundary and loading conditions. The sum of all the individual reactions provides insight into the reaction of the whole [28].

Each small piece is called an element (hence "finite element"), and elements are defined by connection points called nodes. Various elements exist with preferred applications for each. Elements can be one dimensional lines, two dimensional surfaces, or three dimensional solid entities. The segmentation process of the whole into elements is called meshing, and the collection of elements produced is called a mesh.

Higher dimension elements inherently require a higher number of nodes to fully define them but can provide more accurate information. While higher dimension elements can provide improved modeling capability, they can also significantly increase computation time. For example, each node in a 3D beam element can have 6 Degrees of Freedom (DOF) which must be solved for. In order to solve a system of equations, there must be one equation for every independent variable. With many elements each with several 6-DOF nodes, the number of equations can increase rapidly with the number of elements. A more accurate model can also be attained by increasing the number of elements used in the mesh, at the cost of computation time.

Matrices are used to compile and to solve all of these equations. Regardless of the element type, the same fundamental equation is used in structural application.

$$[K]\{D\} = \{R\} \tag{2.6}$$

Where

$[K]$ = global stiffness matrix

$\{D\}$ = displacement vector

$\{R\}$ = load vector

Equation 2.6 is essentially a matrix version of Hooke's Law. The structure is treated as a collection of small springs in static equilibrium. Each element has its own individual stiffness matrix, all of which are incorporated in the global stiffness matrix. Applied loads are accounted for in the load vector. [K] and $\{R\}$ are typically known, so the displacements of each node can be calculated. With knowledge of displacements, geometry, and material properties, stress can be calculated within each element.

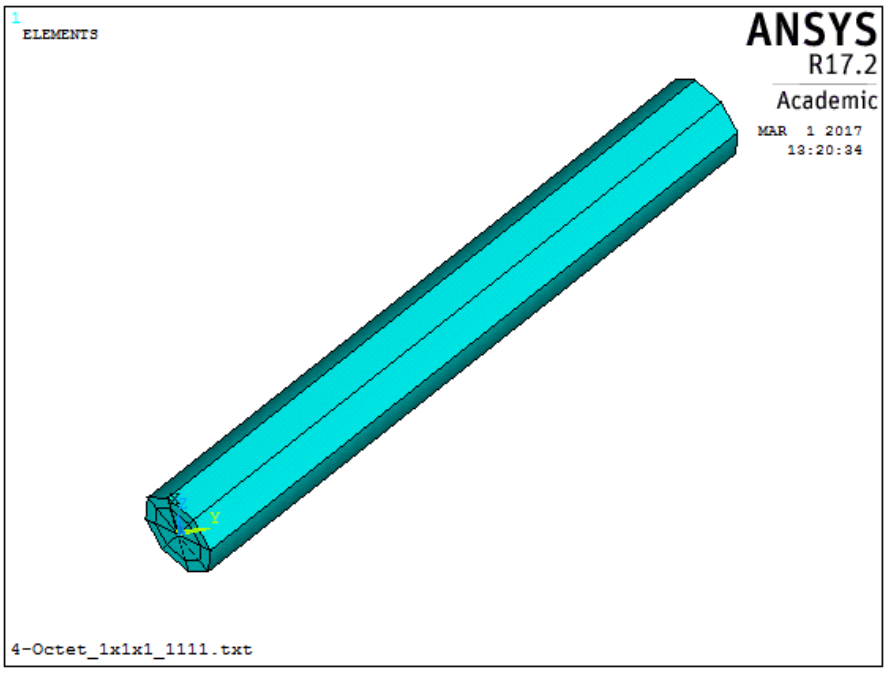

Figure 2.10. ANSYS Beam189 element used to model struts. Thickness shown is for visualization purposes only; beam elements are lines with no physical thickness.

In this study, 3-node, one dimensional beam elements (BEAM189 in ANSYS [29]) are used to represent the lattice struts. It is considered a quadratic element because it can provide a second order response. Each element has a midpoint node which provides displacement information at the middle of each element. Beam elements are a good choice to model struts because they are not computationally expensive but give close approximations to solid elements in the elastic deformation region. The beams are physically represented as one dimensional lines through 3D space. Thickness, cross section shape, and material properties of the struts are accounted for mathematically.

One thing to note is that one dimensional elements do not interact with each other except at specified nodes and connection points. In the model used in this analysis, struts can intersect but not show any deformation or stress as a result. This is a product of the elements being one dimensional.

2.7 Summary

Background and applicable research to periodic cellular lattice materials has been presented. Studies using Finite Element Modeling on compression testing of lattice structures has been presented. Key concepts such as bending vs. stretching-dominated structures and the expected responses of the three selected unit cell types have been discussed. Chapter 3 will outline the methodology used in FEM construction and test conduction.

III. Research Methodology

3.1 Chapter Overview

A scripting method using the software program MATLAB from MathWorks, Inc. and Finite Element Analysis (FEA) program ANSYS Mechanical by ANSYS, Inc. was used to perform the analyses in this study. A review of the program capabilities and the thought process behind building the model will be presented in this chapter. Criteria for experimental lattice specimen selection will be laid out. The methodology for the experimental compression testing of 3D printed Polylactic Acid (PLA) lattice structures will also be outlined.

3.2 MATLAB and ANSYS Collaboration

The basic idea behind a two-program modeling tool is to allow the FEA be performed by a dedicated FEA program and let the iteration and data handling be done by a multifunctional support program. The finite element program ANSYS Mechanical 17.2 was utilized to analyze the lattice structures. ANSYS was used for two main reasons. First, it has the ability to run a scripted analysis, which was necessary in order to iterate through the many combinations of design parameters. Manually producing the desired number of runs from a user interface would be highly inefficient and time consuming. Second, a mature software package was desired to have good confidence in the results.

The ability to script in the ANSYS Parametric Design Language (APDL) allowed multiple autonomous analyses to be performed. The need to autonomously change these APDL scripts was met by using the MATLAB 2016 Student software program from MathWorks Inc. All design parameters are chosen by the user upfront in the MATLAB code, from which numerous analyses can be executed with one click. From

the literature search, it appeared that few studies utilized this software program combination for this purpose or in this manner.

The flowchart in Figure 3.1 gives a top level view of the modeling process. Finite Element (FE) and geometric parameters are defined in MATLAB. Strut and keypoint connectivity is defined to create the aggregate lattice geometry. This data is sent to ANSYS for the FEA portion of the tool. Results of the ANSYS calculations are collected and written to files that are read by MATLAB for data analysis. MATLAB also writes scripts for two software programs to generate the necessary 3D geometry files for printing, which will be discussed in a coming section. These geometry files can be generated without completing a FEA study.

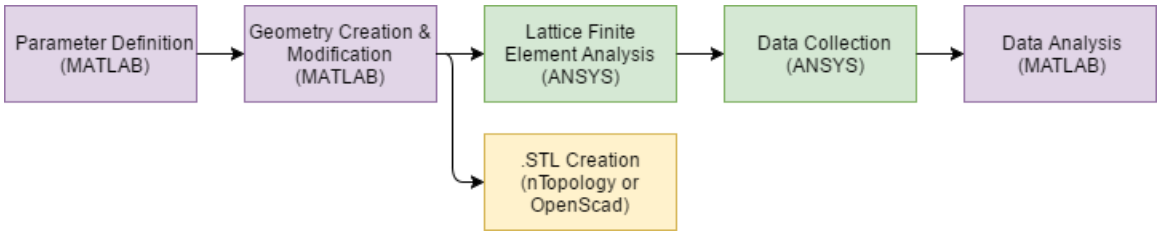

Figure 3.1. Top level flow of the modeling tool.

3.2.1 FE Model Inputs

MATLAB serves as the user interface for the tool. It is responsible for accepting the user inputs for the various parameters. The user has the ability to change geometry parameters for unit cell type, unit cell size, number of cells in x, y, and z dimensions, relative density, strut cross section shape, and amount of imperfection introduced as slight deviations to keypoint locations. The re-entrant strut angle can be changed for Auxetic unit cells. The user can also modify modeling parameters including the type of loading boundary condition (force or displacement), number of elements per strut, and number of load steps. A height in the z dimension can be selected to examine a plot of the stress contour on the lattice cross section at that

height.

The material properties of elastic modulus, Poisson's ratio, density, and yield strength are required for the analyses. If known, a variable elastic modulus as a function of build angle can be input. Otherwise, a constant elastic modulus for isotropic material is used.

3.2.2 FE Model Outputs

The model outputs several values critical to determining lattice performance. Load per mass, with load referring to force or displacement, gives the per-weight ability of the lattice. Force outputs give values pertaining to the structure's strength. Displacement gives values related to compliance of the structure, or its ability to endure strain before yielding. Maximum lattice load (force/displacement), Von Mises stress in the center-most unit cell, and computation time are also collected for each run. These first three primary values (load, load/mass, and stress) are calculated for the exact force or displacement at which yielding occurs. Several other outputs are accessible and used to calculate the primary three.

ANSYS generates data files which are read back into MATLAB for processing. This data is in .txt file format and includes:

- coordinates of undeformed nodes
- x, y, z, and total sum displacements of nodes at last load step
- max stress in each element for each load step
- keypoints and their associated nodes
- elements, their associated nodes, and max stress within them at last load step
- center cell element numbers
- contour plot element numbers

These text files are read in by MATLAB and used for various plots and data management.

Various plots are produced which are discussed later. Three contour plots show the stress in elements at a user-specified z dimension height at yield. Interaction plots are generated for Design of Experiments (DOE) runs to show the effect of a combination of two variables. ANSYS outputs several wireframe images of the last load step deformed lattice.

3.2.3 Model Operation

3.2.3.1 Geometry Generation

MATLAB is used to generate the keypoints and lines that define each lattice, then pass them to ANSYS for analysis. Keypoints and lines for a single cell are stored in a separate function script for each cell. When a given lattice is selected, the appropriate function is called to pass that data to the main MATLAB script. The main script assembles the desired aggregate lattice with user desired attributes. Single cell properties for each cell type are given in Table 2.1.

Aggregate lattice attributes refer to the total number of keypoints, struts, unit cells, and elements that comprise a single lattice. Keypoints and sometimes struts are shared by multiple cells which will affect the total number of that feature. Equations for these are presented here parameterized by the user's inputs for number of cells in each dimension, n_x, n_y, and n_z. Z is defined as the vertical direction. These equations are for ideal lattices without any struts removed.

Equations for BCC:

$$N_{kp} = 2n_x n_y n_z + n_x n_y + n_x n_z + n_y n_z + n_x + n_y + n_z + 1 \tag{3.1}$$

$$N_{strut} = 8n_x n_y n_z \tag{3.2}$$

Equations for Auxetic:

$$N_{kp} = 8n_x n_y n_z + 4n_x n_y + 4n_x n_z + 4n_y n_z + 2n_x + 2n_y + 2n_z + 2 \tag{3.3}$$

$$N_{strut} = 20n_x n_y n_z + 2n_x n_y + 6n_x n_z + 6n_y n_z + n_x + n_y + n_z + 1 \tag{3.4}$$

Equations for Octet:

$$N_{kp} = 4n_x n_y n_z + 2n_x n_y + 2n_x n_z + 2n_y n_z + n_x + n_y + n_z + 1 \tag{3.5}$$

$$N_{strut} = 24n_x n_y n_z + 4n_x n_y + 4n_x n_z + 4n_y n_z \tag{3.6}$$

The equations for number of cells and number of elements apply to all three cell types:

$$N_{cells} = n_x n_y n_z \tag{3.7}$$

$$N_{elem} = N_{strut} N_{div} \tag{3.8}$$

Where

n_x = number of unit cells in the x direction

n_y = number of unit cells in the y direction

n_z = number of unit cells in the z direction

N_{div} = number of divisions (elements) per strut

3.2.3.2 Auxetic Cell Geometric Parameters

As previously mentioned, the Auxetic re-entrant honeycomb cell has variable geometry parameters h, L_{aux}, and θ. To compare with the other two cell types, the choice was made to fix the overall cell dimensions as cubic. The user input of θ, cell size c_s, and the cube constraint defines the values of L_{aux} and h, seen in Equations 3.9 and 3.10, respectively.

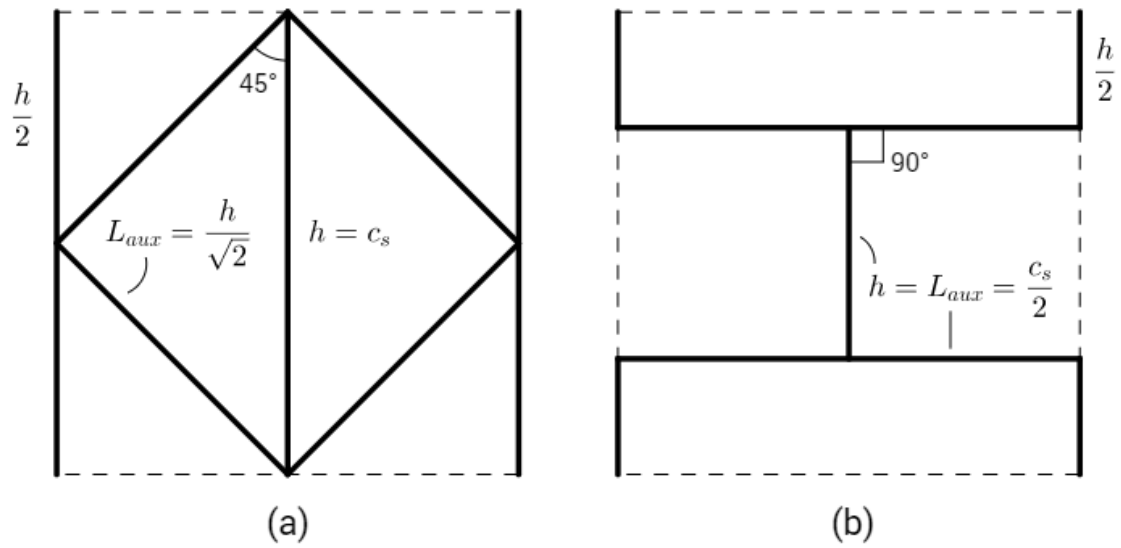

Figure 3.2. Theoretical (a) minimum [45°] and (b) maximum [90°] values of θ for a cubic Auxetic cell.

$$L_{aux} = \frac{c_s}{2\sin(\theta)} \tag{3.9}$$

$$h = L_{aux}(\cos(\theta) + \sin(\theta)) \tag{3.10}$$

θ has a theoretical range of 45° to 90° for a cubic unit cell, as illustrated by Figure 3.2. The realistic minimum value is slightly larger than 45° dependent on the strut thickness. Small angles result in contact between the upper and lower corners of the cell. In this study, two different re-entrant strut angles, 75° and 90° were used in the DOEs. A separate study beforehand studied the effect of the re-entrant strut angle. Methodology for this study is discussed later in this chapter and results are discussed in Chapter 4.

3.2.3.3 Boundary Conditions

The boundary conditions are modeled to mimic the constraints imposed by the universal test machine used for compression testing that can be seen later in Figure

3.13. The machine uses hydraulics to press two parallel aluminum plates together. The compression can be controlled using a force ramp rate or displacement ramp rate. Regardless of control used, all of the top and bottom contact points on the lattice will move simultaneously as the plates compress. This ideology was implemented in the model's boundary conditions.

In the model, the loads are applied to each of the $+Z$ face keypoints in purely the $-Z$ direction. Rigid zero Degrees of Freedom (DOF) boundary conditions are applied to each keypoint at the base of the lattice, at height z=0. ANSYS accomplishes this by applying the boundary conditions to all keypoints at z-dimension heights within the range (desired height)$\pm$(z error). When z-dimension keypoint offset error is introduced, the constraints are applied to the same numbered keypoints as in the unaltered lattice.

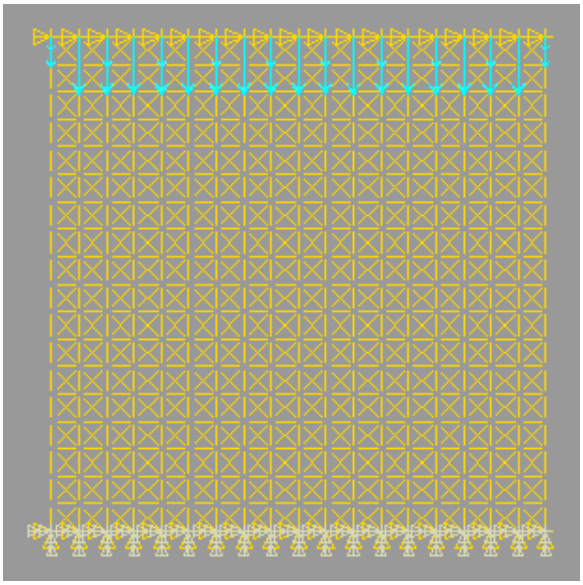

Figure 3.3. Side view of an octet lattice showing modeled boundary conditions. Loads are applied to top face keypoints and 0 DOF contraints are applied to the bottom keypoints. This case shows the differing magnitudes of force loads amongst center, edge, and corner keypoints.

When using force boundary conditions, the user input is treated as the total force and divided proportionately amongst the top face keypoints, dependent on their

location. Keypoints along a top edge receive a load that is half that of a keypoint in the center, and the four corner keypoints receive a load that is one quarter of a center keypoint load. The loads are divided like this to eliminate edge effects that would occur if an equal load was applied to each top face keypoint. In an infinite lattice, a unit cell's top corner keypoint would always be supported by the struts of four unique unit cells. However, in the finite lattices in this study, the top corner keypoints of the aggregate lattice are only supported by one unit cell. Similarly, top edge keypoints are only supported by two cells instead of four. Applying an equal force to each keypoint would lead to higher calculated stress and displacement values that would not be representative of the experimental boundary conditions.

ANSYS incrementally applies the total user-specified force or displacement over a user-specified number of steps. Each load increment is of equal value, load divided by steps. ANSYS will calculate displacements and Von Mises stress values for those specific load increments. The entire simulation is in the linear elastic regime, so ANSYS will report stresses that are greater than the yield stress of the material if the user-specified load causes yield. A breach of yield stress in reality will of course cause non-linear deformation, but modeling as an infinitely linear material allows for the determination of the yield point. MATLAB interpolates the load step stress data to find the exact force or displacement at which yield occurs. To show how this is done, consider Equation 3.11, which defines the uniaxial, elastic displacement of a material block due to an applied force [30].

$$\delta = \frac{PL}{EA} \tag{3.11}$$

Where

δ = displacement

P = force applied

L = length of block in the direction of applied force

E = elastic modulus of the material

A = minimum cross sectional area of the block

Assuming, for a given lattice, that L, E, and A are fixed, it is apparent that $\delta \propto \frac{P}{A}$, i.e. displacement is proportional to stress. Since A is fixed, $P \propto \frac{P}{A}$, i.e. force is proportional to stress. Therefore it can be expected that the stress rises linearly with both force and displacement.

Knowing this, MATLAB interpolates to find the exact load value at which yield stress is breached. First, the load step at which yield has occurred is determined. A ratio between the maximum stress for that load step and the material yield stress is calculated, then used to scale down the stress in every element for the load step. The scaled down values are the stress values at yield, since the highest stress has been scaled down to be exactly at yield. The linearity of the model provides that stress in any one element will be proportional to the stress in another element for any given load.

3.2.3.4 Relative Density and Mass Calculations

Relative density is defined as the density of the lattice structure divided by the density of as described by Equation 3.12. With a constant solid material density, relative density is equivalent to volume fraction. The model takes the user input for relative density and determines the strut diameter that gives that density. Relative density is calculated for a single unit cell by dividing the strut-occupied volume by the volume of a box with the same dimensions as the unit cell.

$$\rho_{rel} = \frac{V_{cell}}{V_{box}} \tag{3.12}$$

Where

V_{cell} = Volume of the unit cell

V_{box} = Volume of unit cell bounding box

To find the single cell volume, the basic approach is to approximate each strut as a cylinder and sum the volumes of those cylinders. This approximation works well for struts with higher length/diameter (L/d) ratios. Overlapping struts at regions near keypoints means that the summation of all of the cylinders' volumes will lead to an overestimate of volume and therefore an underestimate of strut diameter. This is of some concern when working with low L/d ratios or when working in the sub-millimeter range. Strut diameters this small approach the resolution of many commercial 3D printers. A more accurate representation of the volume will calculate a slightly larger strut diameter, which increases the chance of a successful build.

The true overlapping volume of intersecting cylinders is called a Steinmetz solid [31]. The shared volume changes based on the number of intersecting cylinders and the angles at which they intersect. With different cell shapes, strut intersections and angles, it would be difficult to calculate the exact overlapping volume for each intersection. However, as the number of intersecting cylinders approaches infinity, the Steinmetz solid volume approaches that of a sphere. The largest Steinmetz solid (two cylinders) has a volume 1.27 times that of a sphere. Hence, in this study, overlapped volumes were approximated by spheres and removed from the strut volume.

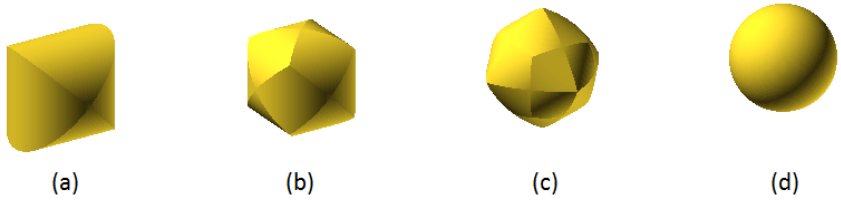

Figure 3.4. Steinmetz Solids created from the overlap of (a) 2, (b) 3, and (c) 4 cylinders. (d) Sphere of same radius for size reference.

The locations of struts and the sphere volumes to be removed both affect the amount of volume that lies within the cell box boundaries. Keypoints and struts shared with adjacent cells also share volumes; therefore, a unit cell that is completely surrounded by other cells must be examined (essentially a 3x3x3 aggregate lattice). A sphere at a unit cell's corner keypoint extends its volume into eight different unit cells. Therefore, the number of sphere volumes to remove from a single unit cell depends on the number of cells the keypoint is shared with. It also depends on the number of struts intersecting. Similarly, a strut shared by N unit cells provides $\frac{1}{N}$ of the cylinder volume to each cell.

Relations between relative density and strut diameter are shown in Equations 3.13 to 3.15. These were each derived by calculating the volume of the cylindrical struts (d^2 term) and subtracting out the overlapped volume (d^3 term). Solving for the strut diameter d requires finding the roots of a polynomial equation.

$$V_{BCC} = \pi d^2 \cdot \sqrt{3} \cdot c_s - 6(2\sqrt{2} - \sqrt{6})d^3 \tag{3.13}$$

$$V_{aux} = \pi d^2(h + 4L) - 2\pi d^3 \tag{3.14}$$

$$V_{oct} = 3\pi d^2 \cdot \sqrt{2} \cdot c_s - \frac{10}{3}\pi d^3 \tag{3.15}$$

Where

$V_{(cell)}$ = Volume of subscripted cell type

$d = d_{solid}$ = solid strut diameter

c_s = cell size

h = Auxetic vertical strut length

L = Auxetic re-entrant strut length

The strut cross section was one more consideration when determining the strut size. This study chose to keep the cross sectional area identical for both solid and hollow struts to see the effect of the hollow struts' greater second moments of area. Fixing the cross sectional area however does not fix the wall thickness, so a consistent $1.25 * d_{solid}$ was chosen for the outer diameter. This mandated the inner diameter be $0.6 * d_{solid}$ for a thickness of $0.325 * d_{solid}$.

Mass is calculated by summing the mass of each individual strut using Equation 3.16. As with strut size, overlapped volumes will cause a slight overestimate of the mass. However, in this case, overlapped regions were not removed. The main reason for subtracting overlapped volumes earlier was to ensure printable strut sizes were created. Adding the masses of the individual struts ensures deleted struts do not get accounted for erroneously. For hollow struts, d^3 is replaced with $(d_o^3 - d_i^3)$, where d_o is the outer diameter and d_i is the inner diameter.

$$m = \sum_{i=1}^{N_{strut}} \rho l_i \pi \left(\frac{d}{2}\right)^2 \tag{3.16}$$

3.2.4 Lattice Analysis Tool Features

Certain key features of the modeling tool will be hit on here. The program consists of a main script and 6 function scripts called from it. This prevents some clutter in the main script and allows for the future addition of new unit cell shapes through addition

of new function scripts. There is one function script for each unit cell type which provides the keypoint locations and strut connectivity for that cell. The other three are function scripts that compose scripts for use in the programs ANSYS, nTopology, and OpenScad.

3.2.4.1 Plots

Three different contour plots give various visualizations of the stress across the lattice cross section at a user-selected height. Values used for these plots are the maximum Von Mises stress from each element that possesses a node closest to the user's selected height. They are plotted with the x-y coordinates of the element's midpoint node. Each plot is three dimensional in the sense that they use x and y coordinate data and plot stress on a third colored "axis", though the scatter plot is a 2D plot with stress values solely represented by color. The scatter plot is most accurate in showing the exact locations of the elements when imperfections are present (both keypoint/node offset error and missing struts). The 3D bar and the 3D surface plots have limited usefulness when keypoint error is introduced due to the MATLAB syntax used to generate the plots. However, they do helpfully display stress trends for lattices with ideal geometries.

MATLAB generates DOE main effect and interaction plots to analyze the importance of variables and the effect of their interactions on lattice performance. Main effect plots show the importance of each factor level, while interaction plots show two-factor interactions. These plots are explained in a later section.

3.2.4.2 Individual Unit Cell Function Scripts

ANSYS needs two sets of data to generate the geometry used in the analysis: 1) x, y, and z coordinates and a number label for every keypoint in the lattice, and

2) the two keypoint numbers which define the endpoints for every strut. Keypoint coordinates and strut connectivity data for a single cell are stored in the unit cell function script and sent to the main script when called. The data is used to create an aggregate lattice according to the user inputs for number of cells in each dimension. The single cell keypoint coordinates and strut connectivity are duplicated along each dimension according to the user inputs. This creates multiple keypoints with the same coordinates for cells with keypoints that are shared with neighboring cells. The duplicate keypoints are then removed and the struts are reassigned with updated keypoint numbers. The final result is the ideal geometry framework for the lattice. Data is stored in matrices until modified by another program feature and sent to the ANSYS script-writer function.

3.2.4.3 Error Offset

Another feature is the ability to insert slight error to the coordinates of each keypoint. A random uniform distribution is used to modify the coordinates of each keypoint up to a maximum distance specified by the user. The user input is in millimeters. Keypoints can be randomly offset in either the positive or negative direction. Coordinate offset in the x, y, and z dimensions can each be individually turned on and/or set to different values. This can be used to mimic the effect of imprecise laser paths or melt pool depths on the as-built geometry. It is shown later that small offsets create struts with stress concentrations which breach yield stress quicker than the ideal geometry.

3.2.4.4 Strut Deletion

Modeling damaged, broken, or improperly built struts can be simulated with the Strut Deletion feature. The user can input a percentage of total struts to be

removed from the lattice. The specific struts removed are again selected using a random uniform distribution, but are limited to struts that are internal to the lattice. Internal struts are defined as struts with no keypoints on any external face. Any internal strut has an equal chance of being deleted. Therefore, the struts selected for deletion from two different runs with identical parameters will almost always be different.

Modeling errors occasionally occur when using this feature due to the random creation of unconstrained struts. The random nature of the strut deletion sometimes leaves a single floating strut disconnected from the rest of the lattice if all of its neighboring struts are deleted. The chance of this happening increases with increasing deletion percentage and decreasing total number of struts. External struts are exempt from deletion, leaving a limited number of struts to choose from for deletion. This tends to occur in Auxetic cells slightly more often, since top and bottom vertical struts are connected to only four other struts.

In practice, the model was restarted whenever this occurred, since the probability of an error reoccurring with a new, randomly generated geometry was low for the chosen parameters. A permanent fix for this would consist of a continuity checker in MATLAB prior to the ANSYS run. For now, a continuity checker is left to future work. In reality, a lattice print with more than a small percentage of struts missing or damaged would most likely be noticed upon inspection and would be reproduced or replaced anyway.

3.2.4.5 Anisotropic Elastic Modulus

The MATLAB code has been written with the ability to incorporate anisotropic elastic modulus values dependent on build angle. For a cylindrical test specimen, changing the angle between the horizontal build plate and the axis of the cylinder

during production produces different material properties, namely elastic modulus. Elastic modulus as a mathematical function of the angle from build plate can be used if desired. Tension/compression specimens at various angles should be printed on the same machine that will be used to create the actual components. An equation for elastic modulus as a function of angle can be generated from that test data and input into the FEA code. In this study however, a constant elastic modulus was used, and study of elastic modulus variations is suggested as future work.

3.2.4.6 nTopology Script Writer

The next two features give the ability to generate the geometry file used by most additive manufacturing (AM) machines. The first program used to do this is nTopology Element, a software package created specifically for generating 3D lattice geometries. MATLAB writes a script defining the keypoints and strut connections. This script is an .xml file type with a .ltcx extension. nTopology reads the keypoints and lines from this file and generates a wireframe lattice. The wireframe lattice can then be thickened, meshed, and saved as an STL file for AM machine use.

3.2.4.7 OpenScad Script Writer

OpenScad is an open source 3D geometry creation software. Geometry is created and rendered using user-generated input code. Basic commands allow creation of simple shapes like spheres, cylinders, and rectangular prisms, and Boolean operations allow combination and manipulation those shapes. This means the geometry can be defined fully with one input script. However, rendering and STL file generation with moderate resolution takes significant time.

To generate a lattice model in OpenScad, a cylinder was rendered for each strut, and a sphere was placed at each keypoint. The keypoint spheres filled in gaps and

rounded off the ends of struts to prevent discontinuities. A resolution of 10 faces around the perimeter of circular areas was used. This means a cylinder is rendered as 10 flat, adjacent rectangular faces around the perimeter with both ends capped.

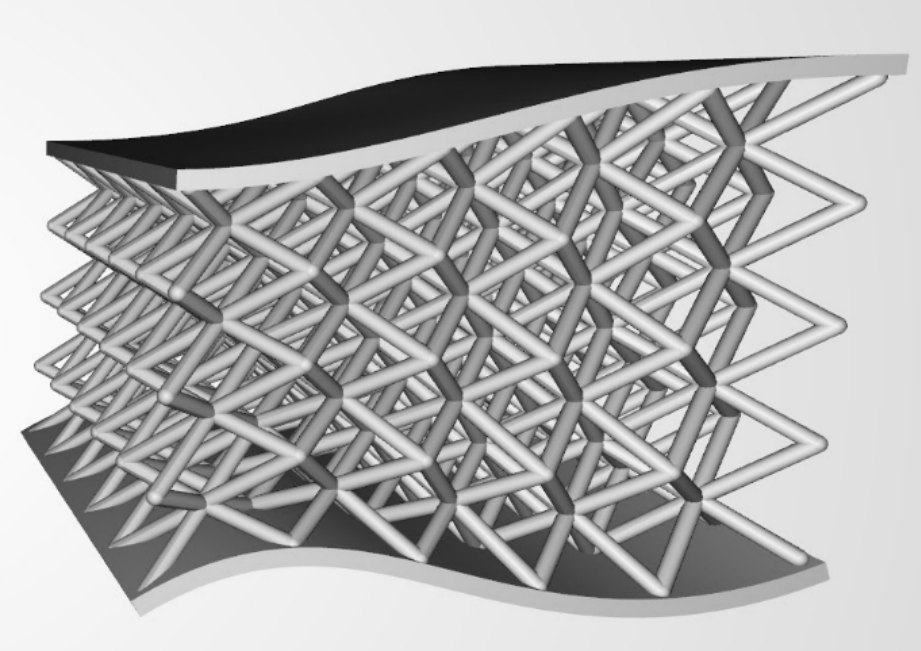

Figure 3.5. nTopology is a lattice generation software with many functions that include creation of conformal lattices to curved surfaces as shown here.

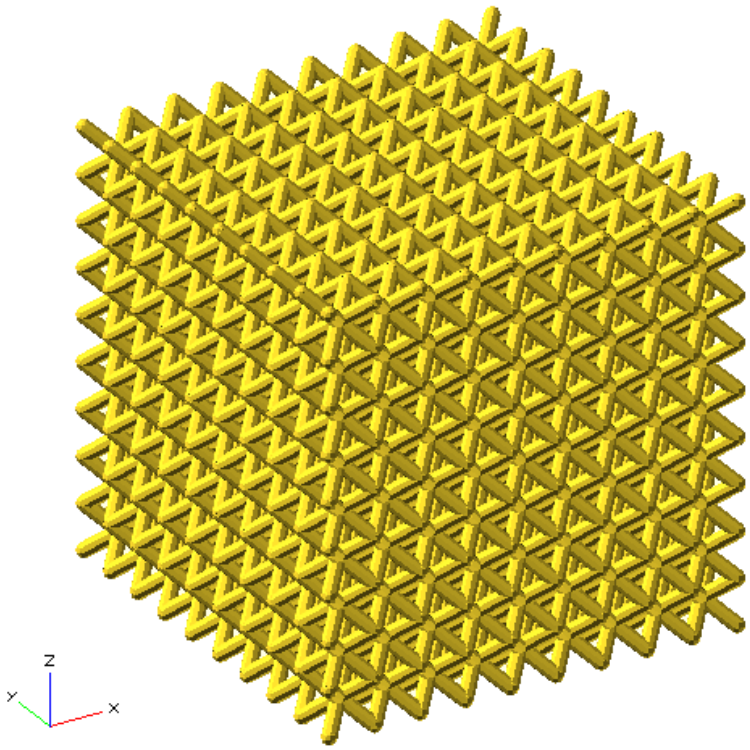

Figure 3.6. OpenScad is a free, code-based, open source geometry generation program that can be used to create 3D print files.

3.2.4.8 nTopology vs. OpenScad

The main difference between these two programs is that nTopology is specifically built and optimized for lattice geometry generation, whereas OpenScad is not. The upside to using nTopology is the speed at which meshes and STL files are generated. Large files on the order of Gigabytes can be processed on the time scale of minutes, where OpenScad would take several hours. One downside is that nTopology requires more user interface time to perform Boolean operations, such as creating hollow lattices. However, nTopology consumes vastly less total time than using OpenScad.

Another difference between the two programs is that strut intersection geometry at keypoint locations is handled differently between the two models. nTopology fillets the intersections of the cylinders, giving a rounded look, while OpenScad uses the

sharper, exact intersection geometry. A comparison can be seen in Figure 3.7. The effect of this was not examined in this study, but it can be reasoned that the extra material around the keypoints added strength by effectively shortening the struts.

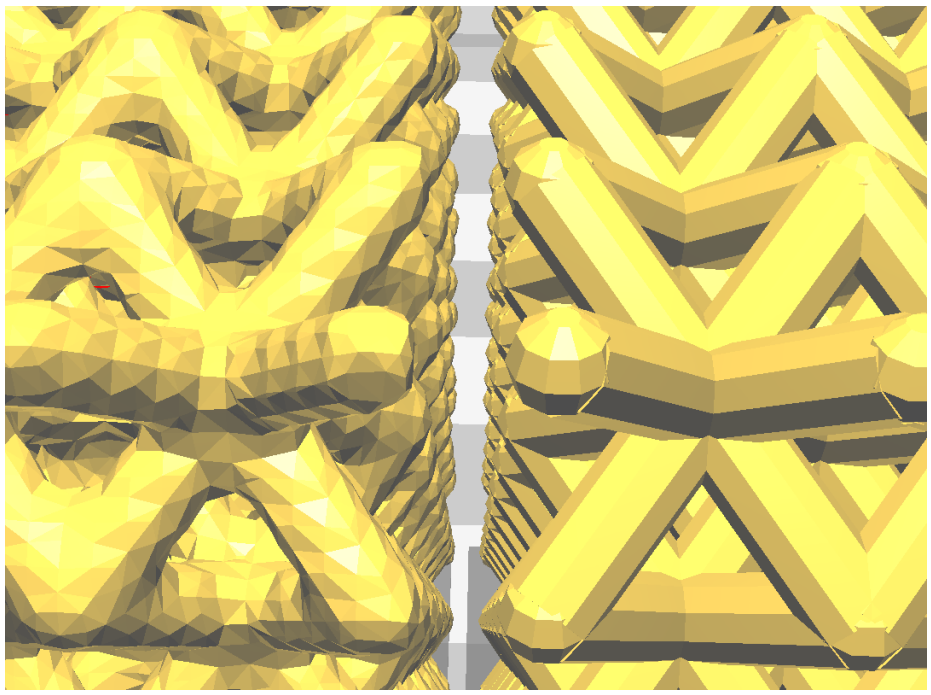

Figure 3.7. Comparison of the STL file geometry generated by (left) nTopology and (right) OpenScad.

3.3 Finite Element Analysis Simulations

3.3.1 Main Study - Full Factorial Design of Experiments

FE simulations were carried out using the model described above. A full factorial Design of Experiments (DOE) was chosen to study the effects of a multitude of design parameters (also called factors) each with a different number of levels. In a full factorial DOE, every combination of factor levels is simulated to examine the impact each factor has on the result in question. The number of runs is given by Equation 3.17. A total of 432 analyses were performed in this study, 216 each for the force and displacement boundary conditions explained in Section 3.2.3.3.

$$N_{run} = \prod_{i=1}^{N_{factor}} k_i \tag{3.17}$$

Where

N_{run} = Number of full factorial runs

N_{factor} = Number of factors

k_i = Number of levels for i'th factor

The factors examined in the study were unit cell type, relative density, strut cross section shape, keypoint offset error, and deleted strut percentage. Various levels were used for each factor and can be seen in Table 3.1. Aggregate size was fixed as a 50 mm, 9x9x9 cube, resulting in a cell size c_s of 5.556 mm. The number of cells was chosen based on the 8-cell minimum recommendation from Andrews et al. [20]. Modeling parameters were set to 1 element per strut and 5 load steps. Examination of these two modeling parameters prior to performing these preceding studies showed no improvement with any higher values.

Table 3.1. Factors and Levels examined in the main DOE.

#	Factor	# Levels	Levels
1	Cell Type	4	1: BCC 2: Auxetic, $\theta = 75°$ 3: Auxetic, $\theta = 90°$ 4: Octet
2	Strut Shape	2	1: Solid Circular 2: Hollow Circular
3	Relative Density (%)	3	1: 10% 2: 30% 3: 50%
4	Keypoint Offset (mm)	3	1: 0 mm 2: 0.25 mm 3: 0.50 mm
5	Strut Deletion (%)	3	1: 0% 2: 1% 3: 2%

The DOE configuration in Table 3.1 was run twice, once for a force loading condition and once for a displacement loading condition. The top load-bearing lattices without imperfection (i.e. without keypoint error or missing struts) were selected from the Force DOE results. Each lattice selected for printing was the highest load bearing solid strut configuration of its cell type, with the 90° Auxetic cell predicted as the overall best solid strut lattice. Both the displacement and force boundary condition studies used the same parameters, however only the unmodified, ideal lattices had the same geometry in both studies due to the random modification features mentioned previously.

3.3.2 Additional Studies

Three additional studies were performed to look slightly more in depth into certain effects.

3.3.2.1 Auxetic Re-Entrant Strut Angle Study

An Auxetic re-entrant strut angle study was performed prior to the main study to see the effect of angle θ on force and displacement performance. Angles of $\theta =$ 55° through 90° in 5° increments were analyzed. Below about 55°, the cubic Auxetic cell approaches the end of its usefulness because the gap between upper and lower struts nears zero, meaning contact will be made quickly under compression. Minimum angle however does also depend on the strut size; thinner struts can be built at slightly smaller angles if desired. All other variables were held constant; values for them are listed in Table 3.2. Both force and displacement boundary conditions were examined. This study was the basis for the inclusion of the 75° and 90° lattices in the main study.

Table 3.2. Parameters and Inputs for the Auxetic Re-entrant strut angle study.

Variable/Attribute	Value
Lattice Cells	9x9x9
Lattice Dimensions	$(50\ \text{mm})^3$
Unit Cell Size	5.556 mm
Strut Type	Solid Circular
Relative Density	10%
Strut Diameter	≈0.6 mm
Offset Error	none
Strut Deletion	0%

3.3.2.2 Keypoint Offset Error Study

A keypoint offset error study looked at larger values of keypoint coordinate error than the main study encompassed. Eight different error levels ranging from 0 mm to 0.8 mm were used. As mentioned previously, the keypoint offset feature is random and can give widely different results from run to run, so an average of five data points for each cell type at each error level was obtained. The force values were normalized with respect to the ideal lattice geometry yield force. Figure 3.3 shows the values for the other variables.

Table 3.3. Parameters and Inputs for the keypoint offset error study.

Variable/Attribute	Value
Lattice Cells	9x9x9
Lattice Dimensions	$(50\ \text{mm})^3$
Unit Cell Size	5.556 mm
Strut Type	Solid Circular
Relative Density	30%
Strut Diameters	BCC = 1.37 mm Aux75 = 1.13 mm Aux90 = 1.19 mm Octet = 0.892 mm
Offset Error	0, 0.1, 0.2, 0.3, 0.4, 0.5, 0.6, 0.7, 0.8 mm
Strut Deletion	0%

3.3.2.3 Strut Deletion Study

Similar to the keypoint offset error study, a strut deletion study looked at lattices with higher percentages of struts removed than the main study had. These two "modification studies" were both performed after the main DOE study. Higher strut deletion levels forced a change in the methodology from what was used in the main DOE. Deletion of any strut in the lattice was changed to delete only completely internal struts.

For the Strut Deletion DOE, eight different levels up to 15% of the total struts were removed from the internal structure. Table 3.4 lists the parameters for all variables used in the study.

Table 3.4. Parameters and Inputs for the strut deletion study.

Variable/Attribute	Value
Lattice Cells	9x9x9
Lattice Dimensions	$(50\ \text{mm})^3$
Unit Cell Size	5.556 mm
Strut Type	Solid Circular
Relative Density	30%
Strut Diameters	BCC = 1.37 mm Aux75 = 1.13 mm Aux90 = 1.19 mm Octet = 0.892 mm
Offset Error	none
Strut Deletion	0%, 1%, 2%, 4%, 6%, 8%, 10%, 15%

3.4 Experimental Compression Testing

This study originally intended to compression test Selective Laser Melting (SLM)-made metal lattices, however circumstances prevented custom metal prints from being produced. As a substitute, PLA plastic lattices were printed on an Ultimaker 2+ Extended 3D printer. Three of each lattice were printed for repeatability.

3.4.1 Lattice Selection

Top performing lattices from the main DOE were chosen for experimental compression testing. The highest load-bearing, solid strut lattice of each cell type was selected. Table 3.5 shows their attributes. Printability was a primary concern; all lattices necessitated printing without support material, because internal supports would be impossible to remove. Solid struts and 50% relative density were chosen in order to avoid feature size limitations of the printer. Strut diameters fell in the range of 1-2 mm, a safe margin above the 0.4 mm nozzle resolution. Figure 3.8 shows 3D models of the three selected lattices.

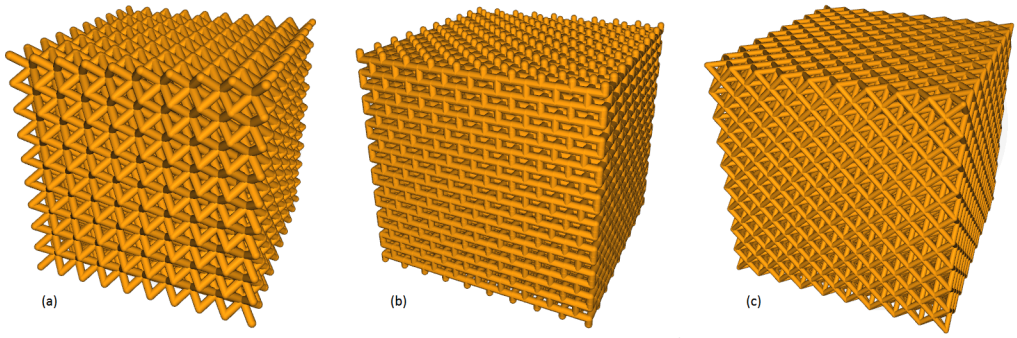

Figure 3.8. 50 mm lattice cubes selected for printing: (a) BCC, (b) Auxetic, and (c) Octet.

One additional consideration for the Auxetic cell was the build orientation required for production. 90° strut angles made it possible to build in the desired crush direction, along the z axis. Auxetic cells with more acute angles have sharp overhangs that create disconnected build layers. The extruder in this case will try to build in mid-air, resulting in excess material strewn across the gap in unintended locations. Though in some cases it may be possible to complete the build like this, the mechanical properties would be greatly diminished. The solution to this is building the lattice on its side. Short horizontal overhangs are possible with the Ultimaker, provided the extruded material is supported on both ends. A downside to side printing would be

the introduction of anisotropic effects from not only the build layer direction but also from the type of plate adhesion. To remain consistent with identical build and crush directions for all cells and to avoid anisotropy, the 90° Auxetic lattice was chosen.

Table 3.5. Lattices selected for experimental testing.

	ID	Cell Type	Strut Type	Relative Density	Offset Error	Struts Deleted	Predicted Force at Yield (N)	Strut Diameter (mm)
1	17	BCC	solid	50%	none	none	2235	1.80
2	19	Aux90	solid	50%	none	none	6011	1.60
3	20	Octet	solid	50%	none	none	5253	1.18

3.4.2 Lattice Generation Methods

Once the three lattices were selected, .STL files were generated with nTopology Element, using the input file generated by the model. The wireframe lattices were thickened to the diameters calculated by the model. Default mesh settings were used to generate the triangular surfaces written to the .STL file ("mesh resolution" and "node smoothing" were set to 0, on a 0 to 1 scale). This default mesh gives an adequate representation of each lattice. Refinement would have generated larger file sizes, which already ranged from 30-150 MB.

The .STL files were then read by Ultimaker's slicing software, Cura, to develop a script readable by the printer. This script, known as "G-code", contains important print parameters and nozzle build path for each layer of the part. The Ultimaker was then used to produce three of each lattice.

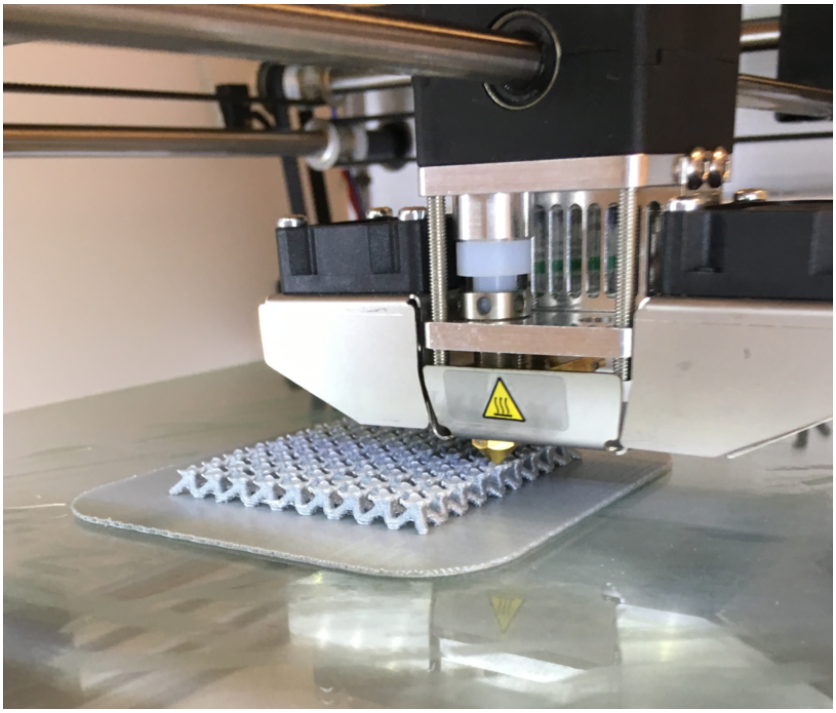

Figure 3.9. BCC cell being produced on the Ultimaker. A raft adhesion technique is shown.

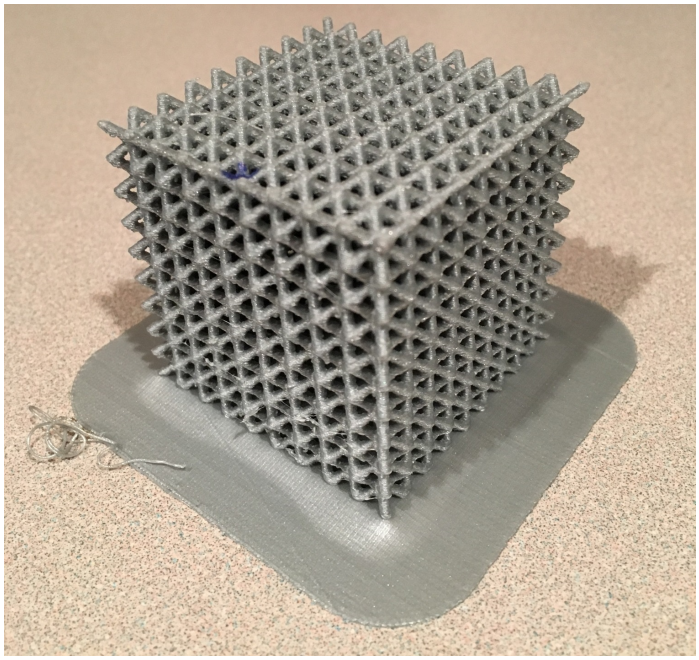

Figure 3.10. As-built BCC lattice used in compression testing.

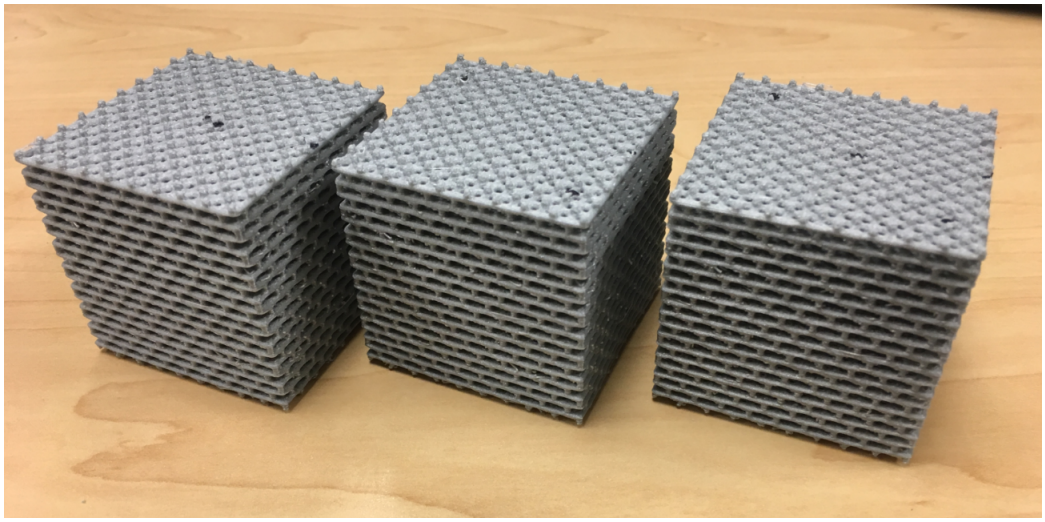

Figure 3.11. Auxetic printed lattices used in compression testing.

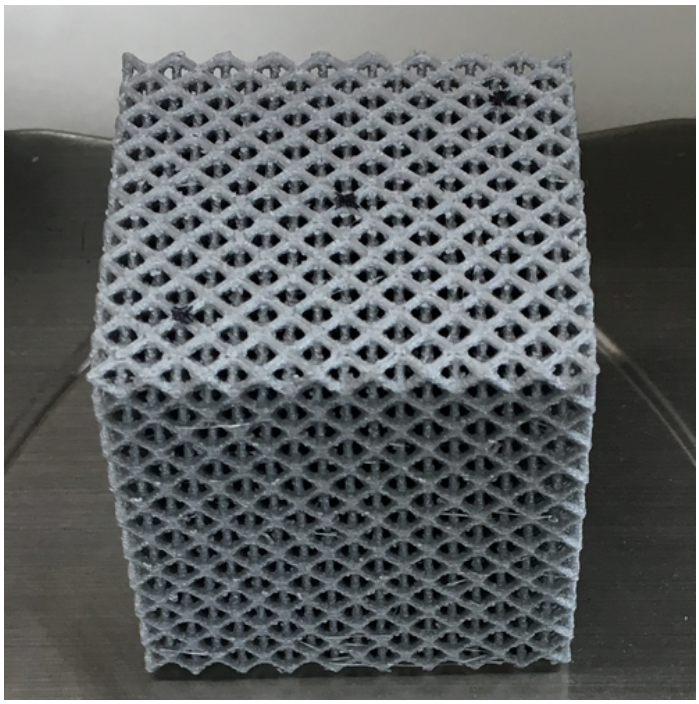

Figure 3.12. Octet lattice used in compression testing.

Print parameters for each cell type are listed in Table 3.6. The octet cell was built with faster settings than the others, though the total print time was the longest at about 25 hours. The Auxetic and BCC cells took about 23 and 15 hours, respectively, but required some parameter changes to prevent build errors. Every strut on the bottom of the octet lattice contacts the build plate, giving it a large, connected surface area with which to adhere to the build plate. Opposite to that, the Auxetic and BCC lattices have small contact surface area at the strut tips. During initial builds of the BCC lattice, the movement of the print head coupled with extrusion of filament disconnected the strut tips from their anchor points. This failure compounded when the separated tips were drug by the nozzle across other tips, disconnecting them as well. First brim and then raft adhesion techniques were attempted, but the problem persisted until the lattice was lowered a fraction of a millimeter and the travel speed of the print head was lowered. Slight variations in raft parameters were used between the Auxetic and BCC lattices.

Table 3.6. Experimental Lattice Build Parameter Settings.

Cell Type	BCC	Aux90	Octet
Layer Height (mm)	0.15	0.15	0.15
Infill Density	100%	100%	100%
Print Speed (mm/s)	60	60	60
Travel Speed (mm/s)	100	80	150
Support	none	none	none
Build Plate Adhesion	Raft	Raft	Skirt
Raft Air Gap (mm)	0.3	0.2	N/A
Initial Z overlap (mm)	0.15	0.1	N/A
Raft Top Layers	2	2	N/A

3.4.3 Lattice Compression Tests

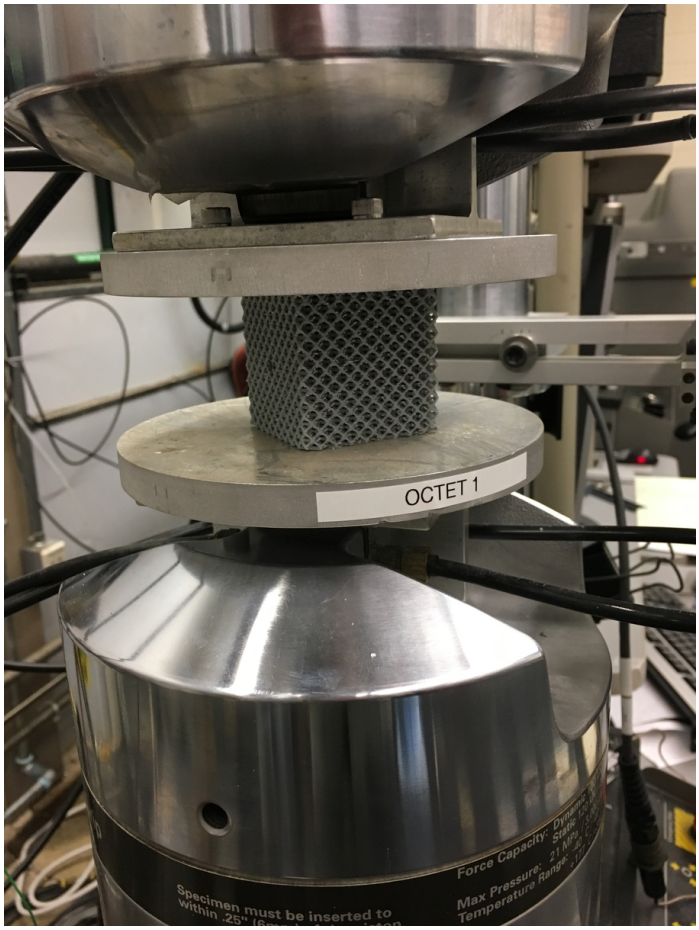

Figure 3.13. Experimental setup on Test Machine.

A 22 kip MTS 793 Universal Test Machine was utilized to compress the test specimens. Lattices were compressed between two parallel aluminum platens. The hydraulic heads were operated by a controlled displacement value and logged output data for concurrent force and displacement. On this machine, the bottom platen moves upward to compress the specimen against the fixed top platen. Force and displacement were sampled every 0.1 seconds. The compression rate was a ramp input at 0.1 mm/s up to a total displacement of 12.5 mm. This rate was selected to provide a quasi-static load relatively free of inertial effects.

All lattice specimens were crushed in the build direction. More precisely, the

crushing direction was normal to each build layer of the part.

Three of each cell type were compressed using this process. A data recording issue required a 4th Auxetic, and 10th overall lattice to be crushed. Video of each test was recorded using a GoPro Hero 3+ camera. Pictures were taken throughout the process, including one of each side face post-crush.

3.4.4 Data Analysis

The output force vs. displacement curves for each lattice were analyzed individually. First, the point at which the lattice first contacted the upper platen was determined. The machine displacement was zeroed out such that the distance between the platens was very nearly the height of each lattice. However, due to slight variability in the lattices, and to be able to place new specimens on the platen, a small gap on the order of 0.1-0.2 mm was left between the lattice and upper platen. The force reading was also zeroed out at this non-contact point. In order to remove this gap from the data, an average of the force reading was found for the unloaded load cell. Although the force reading was zeroed, the resolution still caused the output to jump around by tens of Newtons. In the first few seconds of the run, no load was applied because the lattice was not yet touching the top platen. Once contact was made however, the force reading began to rise. The point at which the force reading stayed above the average no-load force reading was taken as the true zero displacement point. All displacement values were lowered by the displacement value at this point.

Next, the overall lattice stiffness, K, was determined. This is the slope of the linear region on the displacement-adjusted force-displacement curve. A displacement range was selected well within what appeared to be the linear region. The same range for each cell type was used when possible; BCC 1 used a slightly smaller range than the

other two BCC specimens because a slight non-linear portion of the curve appeared to show yield at a lower displacement. A linear best fit line was applied to the data points in that displacement range. The slope of the best fit line is the stiffness, K. The equation defines the linear region and is used to determine the equation of the 0.2% offset line. This 0.2% strain is commonly used in material testing to designate the onset of yield [30]. It is a line with slope K that is horizontally offset from stress-strain data by 0.002 $\frac{\Delta L}{L}$. This is normally applied to stress-strain data, so it is reverse engineered to calculate the appropriate line on a force-displacement graph. Equation 3.18 calculates the new y intercept value for the offset line:

$$b_{new} = b_{old} - 0.002KH \tag{3.18}$$

Where

b_{new} = y intercept of the 0.2% offset line

b_{old} = y intercept of the experimental data's linear region

K = experimental stiffness of lattice

H = height of lattice in crush direction

The equation of the offset line is then:

$$F = K\delta - b_{new} \tag{3.19}$$

Where

F = Force

δ = Displacement value

The first data point where the offset line is greater than the experimental data is defined as the yield point. The displacement and force data at that point is then

divided by the measured lattice mass to get the per-unit-mass values. The data is averaged across the three runs and the standard deviation is found. These average values are then compared to the model DOE results.

Ashby [1] presents a log-log plot of relative elastic modulus against relative density. On this plot, he shows lines of ideal bending and stretching-dominated behavior, along with typical ranges for a number of lattice and foam families. For the experimental lattices, the elastic modulus is found for each specimen from the experimental stiffness using the relationship in Equation 3.20:

$$E = \frac{KH}{A} = \frac{K}{H} \tag{3.20}$$

Where

E = experimental Elastic Modulus

$A = H^2$ = cross sectional area of the lattice bounding box

Following this, the elastic modulus values and experimental relative densities for each cell type were averaged. The relative elastic modulus is then found by dividing the average elastic modulus by the Ultimaker-published value for the PLA (see Table 3.7). The relative values for elastic modulus and relative density were compared to ideal and then plotted on the graph presented by Ashby to visualize the comparison.

Table 3.7. Material Properties of Ultimaker PLA [3].

Modulus of Elasticity (Pa)	2.85E+09
Poisson's Ratio	0.36
Specific Gravity	1.24
Density (kg/m^3)	1239.965
Yield Strength (Pa)	3.81E+07

All of these plots and values are presented in the next chapter.

3.5 Summary

This chapter laid out the process for evaluation of lattice structures and their properties through use of a tailored FEA tool. Considerations and thought processes for tool development were outlined. The results from the studies mentioned here will be discussed next. The experimental results for compression tests of the selected lattices will also be included in the next chapter.

IV. Results

4.1 Chapter Overview

This chapter will present the results from the simulations run via the model and from the experimental compression testing of additively manufactured lattice cubes. On the simulation side, four extensive studies were conducted. The Auxetic strut angle study looked at the effect of different angles of θ on the Auxetic cell response, and facilitated the selection of two cell shapes used in the main full factorial design of experiments. Following the primary study, two lattice modification studies were performed, looking at keypoint offset error and strut deletion. On the experimental side, the results of compression testing three different unit cell lattice cubes are examined and compared to the predictions from the model.

4.2 Simulation Results

Three simulations were conducted to provide input to or expand upon results of the main Design of Experiments (DOE) study. The effect of strut angle θ was examined in a study prior to the main study. The main study itself examined the trends among five variables: cell type, strut type, relative density, offset error, and strut deletion. Offset error and strut deletion variables were examined further to characterize their effects.

4.2.1 Auxetic re-entrant cell angle DOE

Results are shown in Table 4.1, and Figures 4.1 and 4.2. The model predicts the greatest load bearing capacity and displacement magnitude when the re-entrant struts are oriented horizontally, that is, when θ=90°. Force steadily drops between the highest and lowest angles while displacement decreases with decreasing angle and

bottoms out between 60° and 65°. Angles closer to the extremes are expected to compress the most before yielding. In this case, 90° has highest displacement before yield. Because of its dominant predicted performance, the 90° lattice was chosen to take part in the main DOE. Another angle, 75°, was also chosen to examine the properties of a non-orthogonal Auxetic cell in comparison to the 90° lattice.

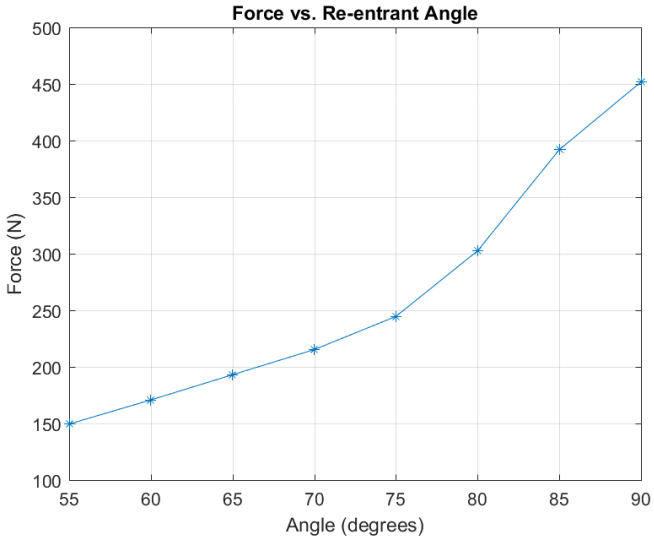

Figure 4.1. Effect of angle θ on load bearing capacity of Auxetic re-entrant cell.

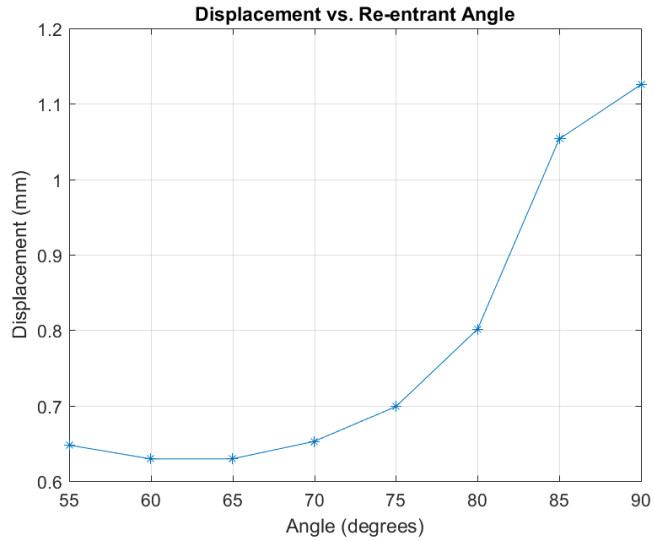

Figure 4.2. Effect of angle θ on displacement before yield of Auxetic re-entrant cell.

Table 4.1. Force and Displacement at yield results from re-entrant angle study.

θ	Yield Force (N)	Force per mass (N/kg)	Yield Disp (mm)	Disp per mass (mm/kg)
55°	149.4	8449	0.648	36.61
60°	170.7	9593	0.629	35.35
65°	193.0	10781	0.629	35.15
70°	215.2	11955	0.652	36.25
75°	244.5	13518	0.699	38.62
80°	302.6	16655	0.801	44.11
85°	391.9	21500	1.053	57.79
90°	451.8	24719	1.126	61.59

4.2.2 Main Study - Full Factorial Design of Experiments

As discussed in Section 3.3, the main DOE study encompassed the 3 main cell parameters (cell type, strut type, and relative density) and 2 modification parameters (keypoint offset error and strut deletion). A full factorial design was chosen to examine the effects of all parameters against all others. A full factorial DOE gives good trend analysis to show the most important factors in determining lattice strength. Table 3.1 shows the number of levels and values for those levels for each variable. Every lattice studied was a 9x9x9, 50 mm cube with 5.556 mm unit cell size.

Figures 4.3 to 4.6 show the effect of each factor on the four main response variables at yield, which are displacement, displacement per mass, force, and force per mass respectively. In these plots, the average force or displacement value for each factor level is plotted, distinctly showing differences amongst the various levels of a given factor.

Trends for each of the factors are seen in these plots. A comparison of cell types reveals that the Octet cell on average displaces the least and can carry the highest load, indicating a higher stiffness than the others. On the other hand, the BCC cell is the weakest but has the highest displacement to mass ratio, indicating better energy absorption per weight. The 90° Auxetic cell claims highest displacement at yield. It

also beats its 75° counterpart in all 4 categories.

Hollow struts are predicted to have higher values in all four categories. With the same relative densities, both struts have the same cross sectional areas, but the hollow struts benefit from a higher second moment of area. Axial displacements are the same, however the higher second moment allows them to support more bending load in the bending-dominated cells.

Relative density has a significant difference between levels on all plots. As one would expect, it shows that higher relative densities displace less and can carry more force, indicating higher stiffness.

The modification factors of keypoint offset error and strut deletion show similar trends with different magnitudes. Both indicate weaker lattices with the imperfections, but keypoint error shows a drop much larger than strut deletion. The most significant drop occurs between no error/deletion and the first level of each factor. The average values appear to level out after this initial drop. Whether that is a characteristic of the imperfections or due to a very small change in the error levels is examined more in depth in the two follow on studies.

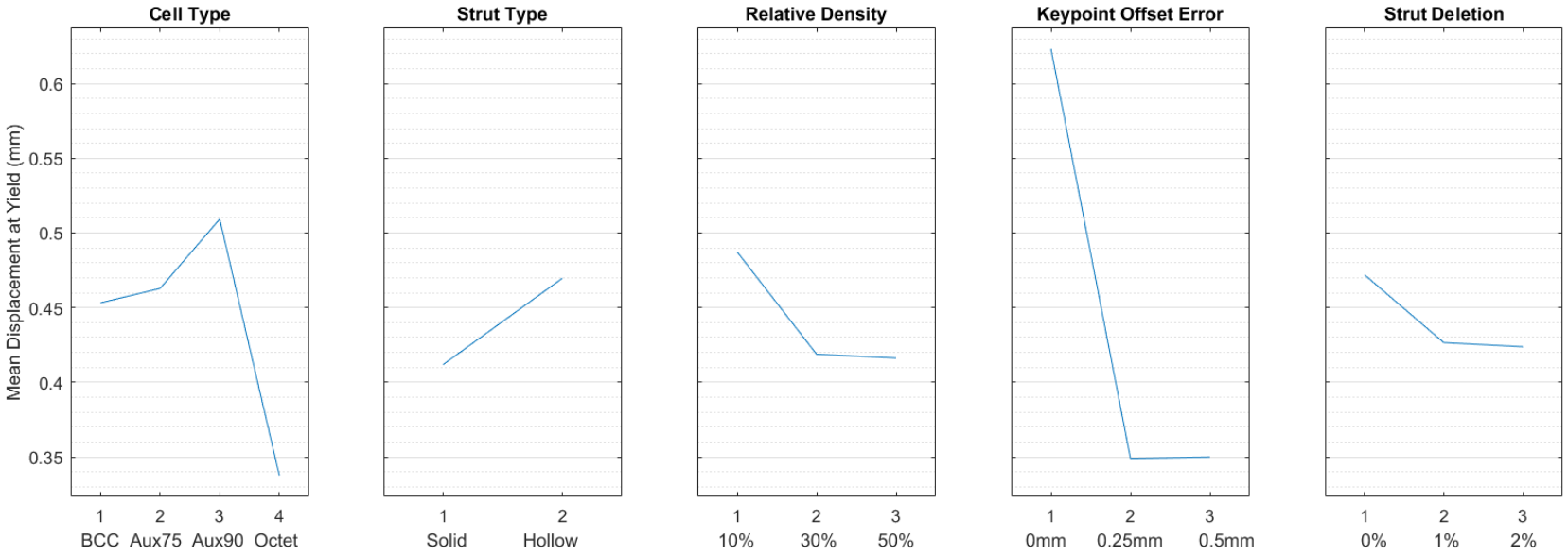

Figure 4.3. Main Effect Plot for Displacement at Yield.

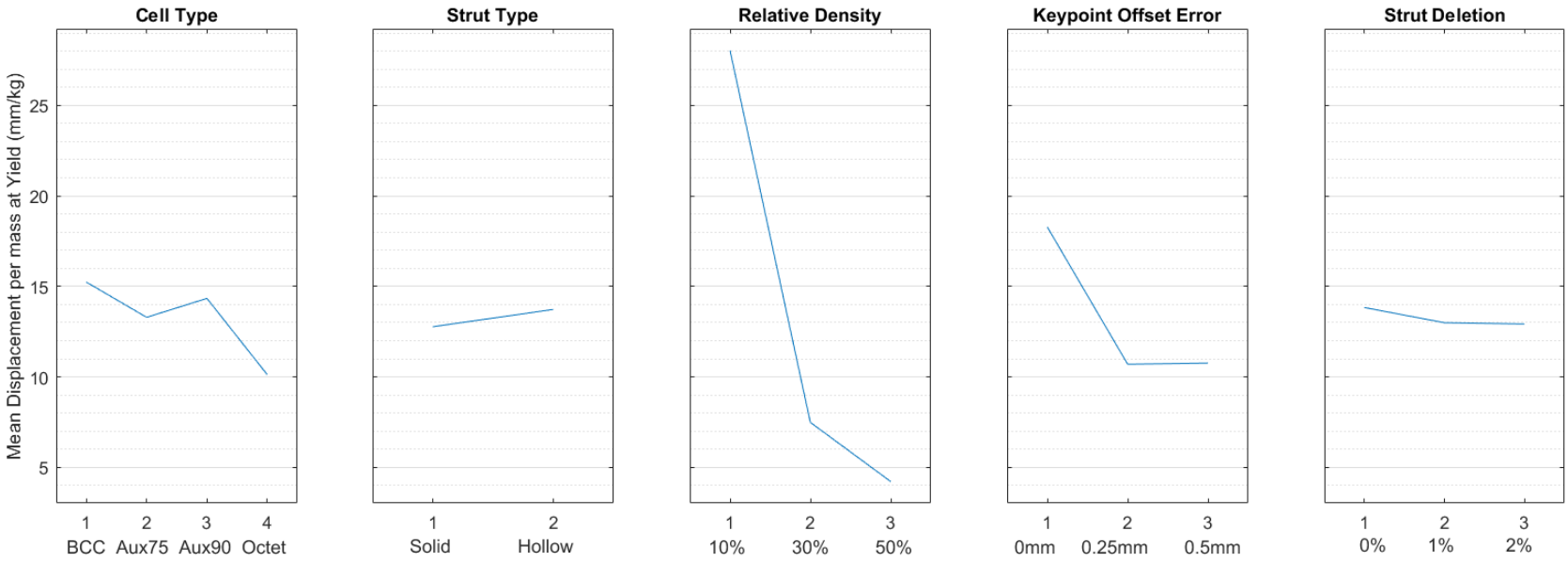

Figure 4.4. Main Effect Plot for Displacement per mass at Yield.

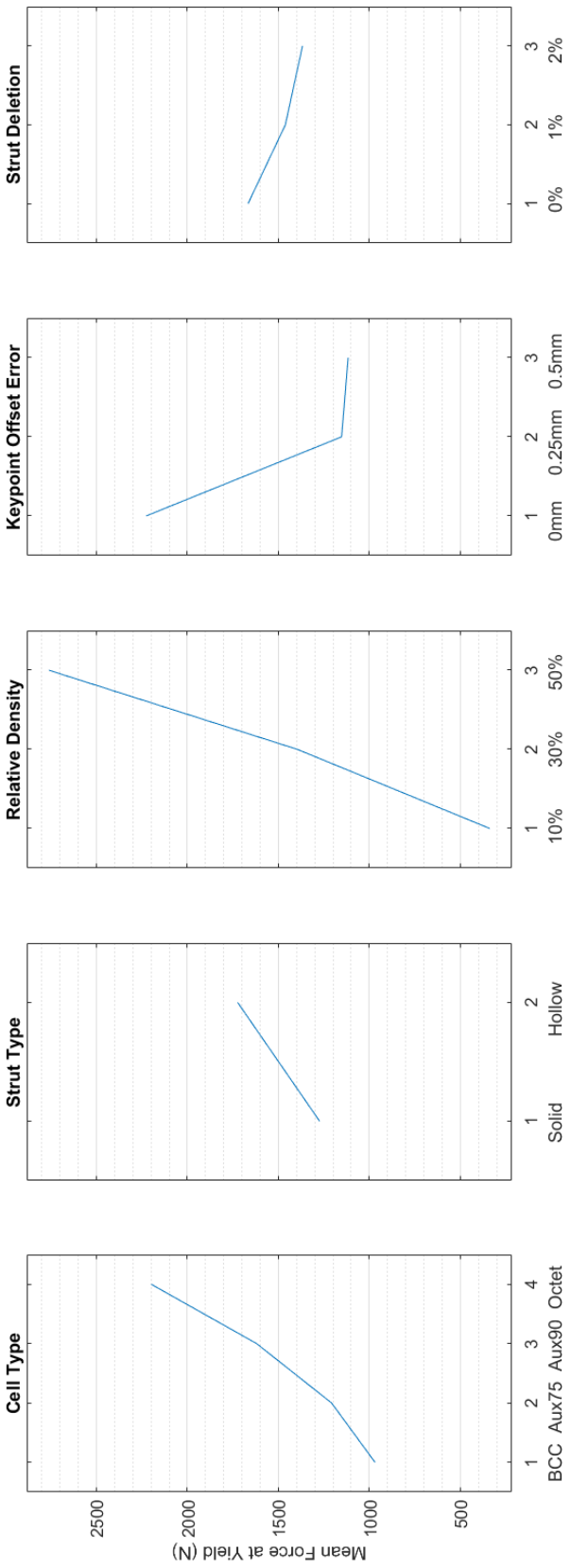

Figure 4.5. Main Effect Plot for Force at Yield.

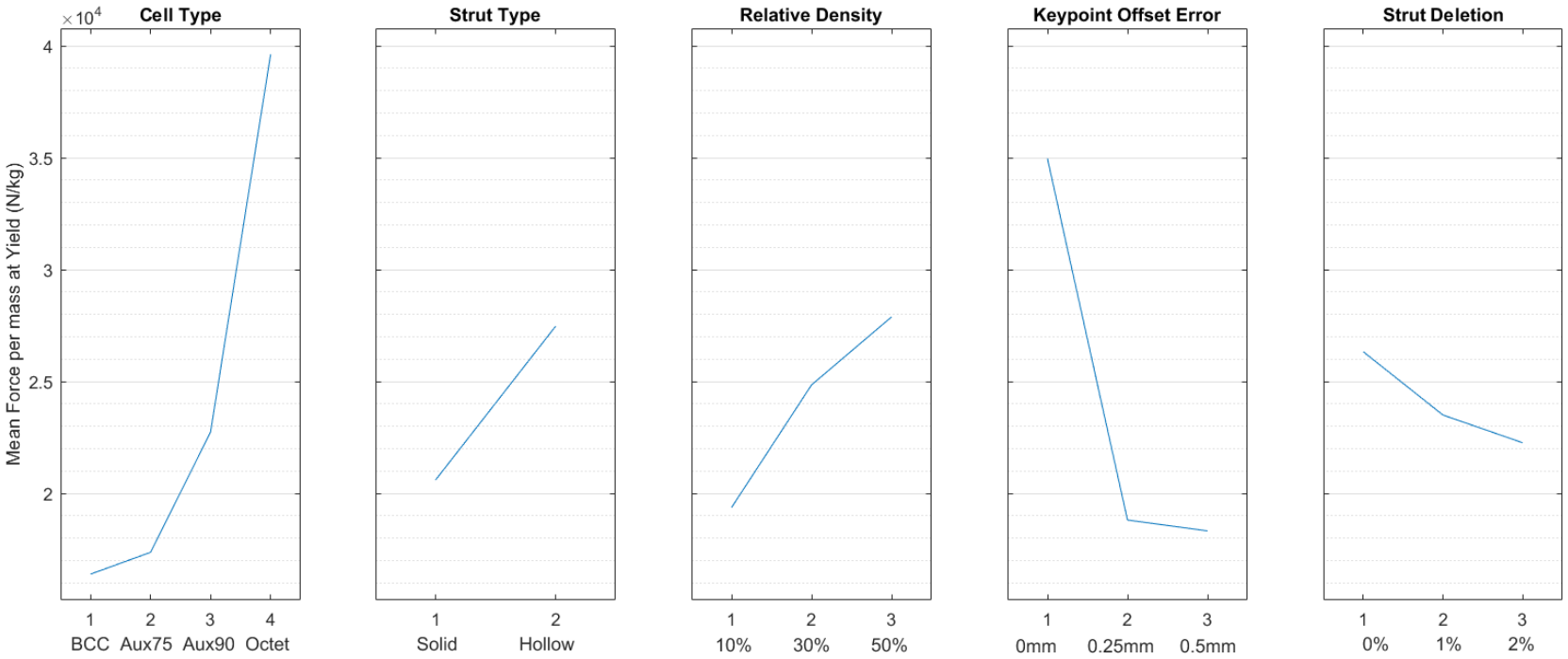

Figure 4.6. Main Effect Plot for Force per mass at Yield.

An examination of only the runs without any imperfections reveals an interesting switch in overall performance. Figure 4.7 show the Force and Force per mass main effect plots for cell type. With the imperfection runs included, the Octet-truss was far superior in both Force and Force per mass categories. However, the average ideal 90° Auxetic lattice can carry more load than the ideal octet-truss lattice. This indicates that the Auxetic cell is much more sensitive to imperfections than the other cell types, especially the octet. Strut type and relative density factors showed similar trends in both ideal and non-ideal runs.

The Auxetic 90° also becomes the lattice with expected highest displacement per mass, surpassing the BCC cell, seen in Figure 4.8. Displacement predictions showed the same trends for both ideal and non-ideal, with the Auxetic 90° having the highest average values. Just like the force analysis, changes to strut type and relative density effects were not evident when looking only at ideal lattices.

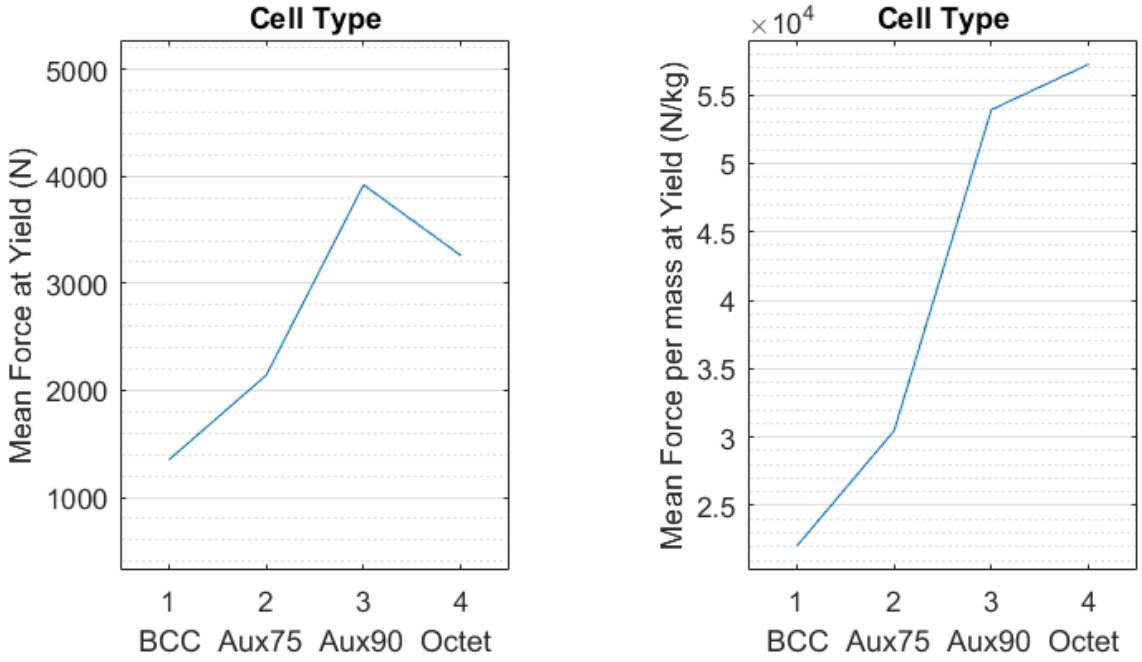

Figure 4.7. Cell Type Main Effect Plots for Force and Force per mass at Yield, including only ideal lattice geometries. Note that in the ideal case, the bending-dominated Aux90 cell is predicted to carry higher load on average than the stretching-dominated octet.

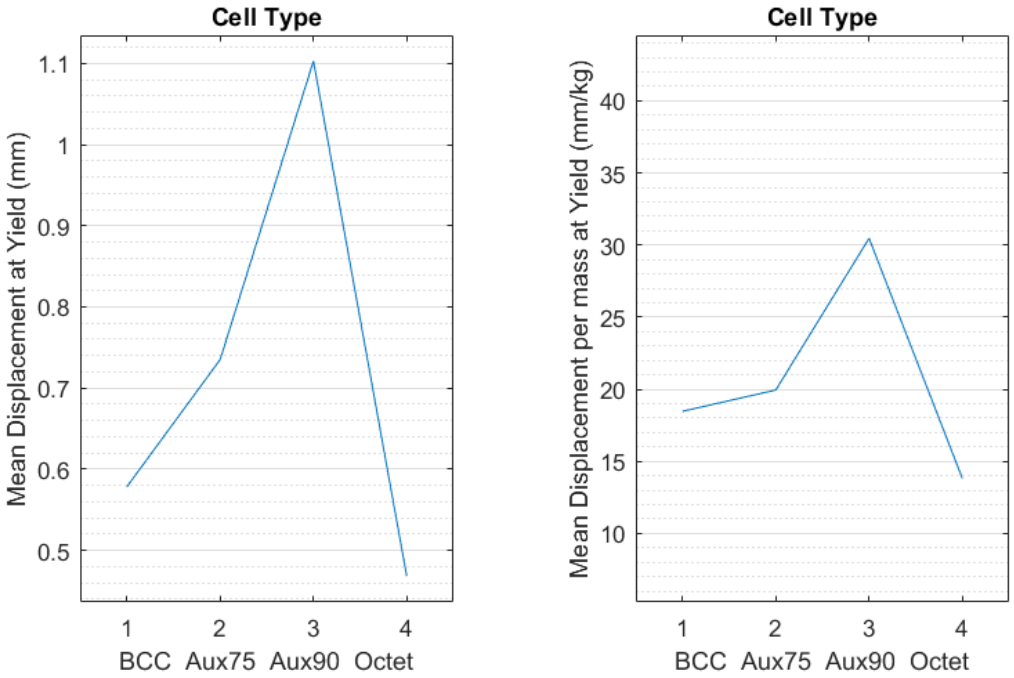

Figure 4.8. Cell Type Main Effect Plots for Displacement and Displacement per mass at Yield, including only ideal lattice geometries. Note that in the ideal case, the Aux90 cell is predicted to have a higher displacement per mass on average than the BCC cell, which had the highest values when imperfections were included.

The top 5 overall best force load bearing lattices and their parameters are shown in Table 4.2. Surprisingly, the model predicted that the strongest lattice configurations were Auxetic cells with 90° struts rather than the octet cell. The Aux90 cell excelled in both force and force per mass categories. Trends noticed here are that the top lattices all have the highest density of 50% and no keypoint error. A more interesting outcome is that two of the top 5 are missing struts. It is plausible that removing struts could relieve stress in some cases, like in the over-constrained/self-stressed octet cell, but the result is still intriguing and warrants further study. The top two lattices shared identical geometry, the only difference being that second place had 1% of the struts removed.

Table 4.3 shows the best force per mass lattices. Three are also in the top 5 for force. Similar cell and strut types show up. One octet has 2% of struts deleted, but

Table 4.2. Top 5 Load Bearing Lattices from Force DOE.

	ID	Cell Type	Strut Type	Relative Density	Offset Error	Struts Deleted	Force at Yield (N)
1	23	Aux90	hollow	50%	no error	none	9522
2	95	Aux90	hollow	50%	no error	1%	6230
3	19	Aux90	solid	50%	no error	none	6011
4	24	Octet	hollow	50%	no error	none	5942
5	168	Octet	hollow	50%	no error	2%	5776

other than that there are no imperfections. The first two are again Aux90 cells and are identical except for one parameter, which is relative density this time. However, it appears as though relative density is not quite as important as it was for force alone.

Table 4.3. Top 5 Load Bearing per Mass Lattices from Force DOE.

	ID	Cell Type	Strut Type	Relative Density	Offset Error	Struts Deleted	Force per Mass at Yield (N/kg)
1	23	Aux90	hollow	50%	no error	none	88640
2	15	Aux90	hollow	30%	no error	none	70308
3	24	Octet	hollow	50%	no error	none	60530
4	168	Octet	hollow	50%	no error	2%	60032
5	4	Octet	solid	10%	no error	none	58679

Another way to visualize the effects of variables is to look at the interactions between each combination of two variables. Figures 4.9 and 4.10 show interaction plots for force and force per mass results, respectively. In Figure 4.9, the y axis is force at yield. The x axis changes with the variable. Each subplot is similar to elements in a symmetric matrix; e.g. subplot (2,1) displays the same data as subplot (1,2), but with different connectivity. Trends can be observed by looking at 1) the slope of the lines and 2) the vertical distance between the lines. Lines with greater slope mean the parameter in that column has greater effect on the force value than those of less slope. Lines with greater vertical distance between them show a greater force dependence on the parameter in that row. Two factors with identical effects would show overlapped, horizontal lines.

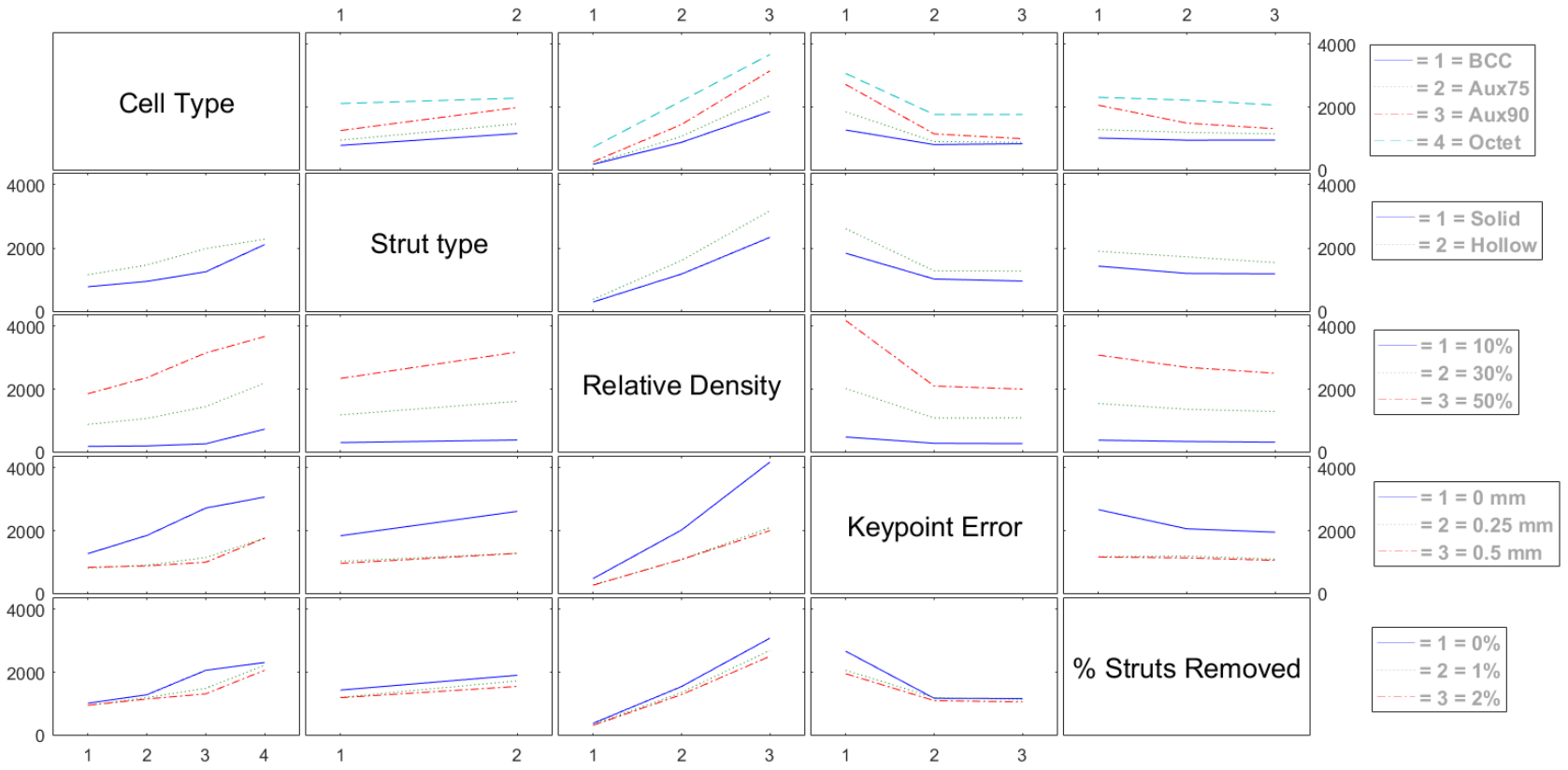

Figure 4.9. Force Interaction plot

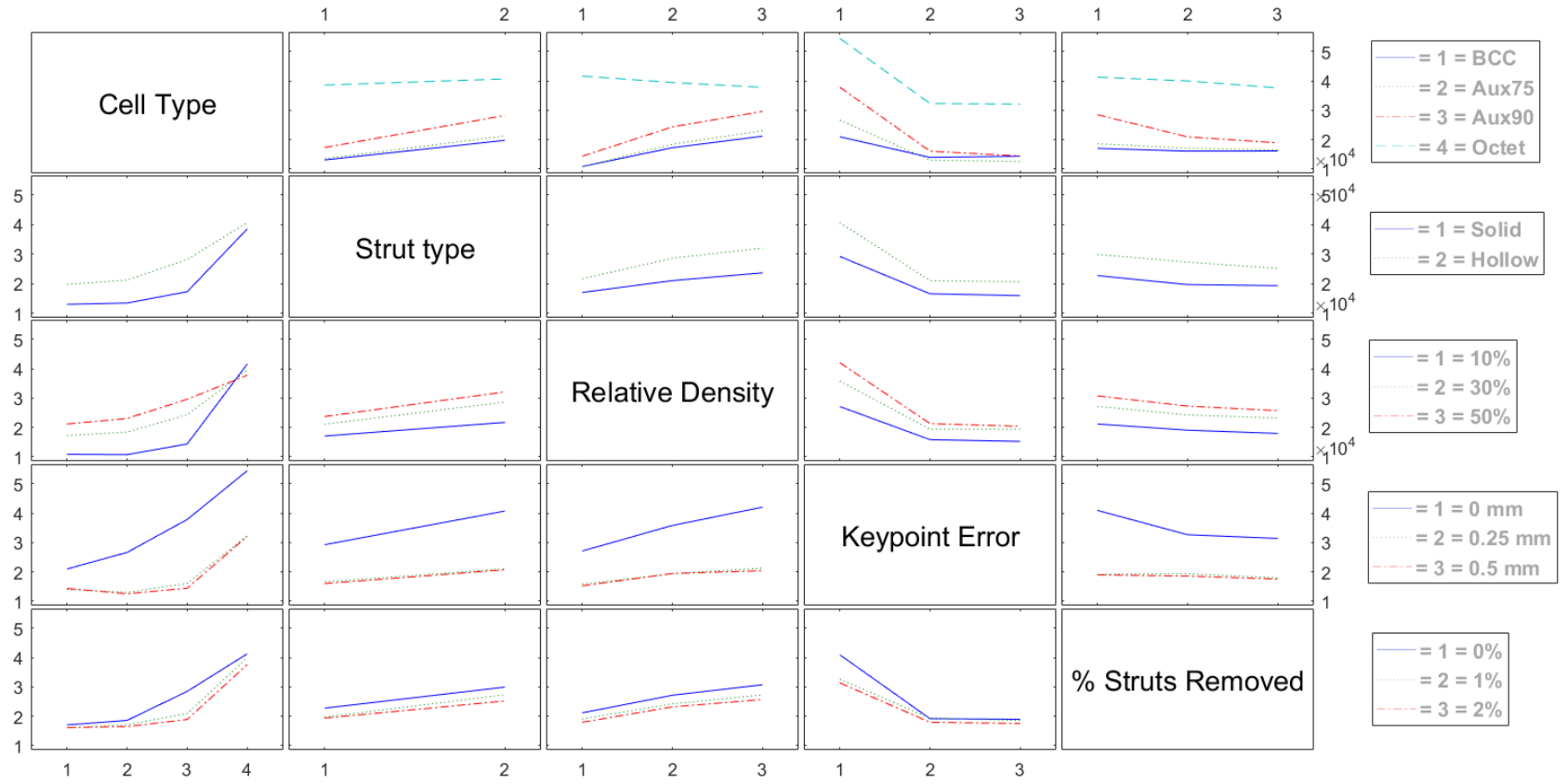

Figure 4.10. Force per mass Interaction plot

As an example, a parameter with evident effects in these interaction plots is relative density. Large slopes on all of the subplots in the relative density column show that the yield force changes drastically with the relative density level (levels 1,2, and 3 correspond to 10%, 30%, and 50% respectively). Similarly, each plot in the relative density row shows lines with significant vertical separation, indicating a difference in force. In each case, the red line, corresponding to 50% relative density, is the highest load no matter which other parameter level relative density is combined with.

Displacement results don't give true indications of the strength of the lattice, but rather help to understand the compliance of the structure, and in turn, energy absorption characteristics. In general, results show that the bending dominated structures displace more before yielding than the stretch dominated octet-truss. The three most and three least compliant structures are shown in Table 4.4.

Table 4.4. Lattices with the 3 Largest and 3 Smallest Displacements at Yield.

Rank	ID	Cell Type	Strut Type	Relative Density	Offset Error	Struts Deleted	Displacement at Yield (mm)
1	23	Aux90	hollow	50%	none	none	1.306
2	15	Aux90	hollow	30%	none	none	1.215
3	7	Aux90	hollow	10%	none	none	1.202
214	138	Aux75	solid	50%	.5 mm	1%	0.237
215	68	Octet	solid	50%	.5 mm	none	0.216
216	140	Octet	solid	50%	.5 mm	1%	0.216

Displacement per mass at yield is shown in Table 4.5. The lighter structures with 10% density move up the list to be the configurations with the highest displacements per mass. The same three lattices remain at the bottom, with the bottom two swapping positions.

The low end values mean one of two things, either 1) the lattices are incredibly stiff, or 2) strange geometry caused yielding to occur quickly. The model used for the main DOE was able to randomly create strut arrangements that artificially induce

Table 4.5. Lattices with the 3 Largest and 3 Smallest Displacements per mass at Yield.

Rank	ID	Cell Type	Strut Type	Relative Density	Offset Error	Struts Deleted	Displacement per Mass at Yield (mm/kg)
1	7	Aux90	hollow	10%	none	none	65.77
2	3	Aux90	solid	10%	none	none	61.59
3	75	Aux90	solid	10%	none	1%	42.50
214	138	Aux75	solid	50%	0.5 mm	1%	2.31
215	140	Octet	solid	50%	0.5 mm	1%	2.22
216	68	Octet	solid	50%	0.5 mm	none	2.20

high stress, such as the one shown in Figure 4.11. Figure 4.11 shows a cantilever top corner strut that is normally supported by two other struts. Because a load is applied to the top corner keypoint, the strut sees much higher stress than it typically would. The model predicts that the strut will yield quickly in this case, when in reality the strut would see nearly no stress when the entire top surface is compressed by the flat platen of the test machine. This can be considered an artificial yield scenario generated by the boundary conditions. It is possible for random deletion and keypoint movement to cause high stress concentrations that are not seen in ideal versions of the same lattice, but this is the expected effect and different from the artificial scenario described above.

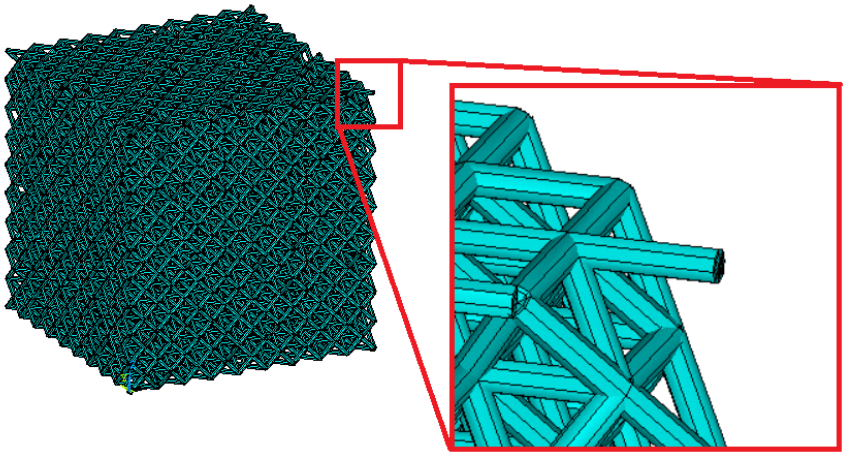

Figure 4.11. Cantilever strut on top corner of an Octet lattice.

A drastic drop in performance due to an artificial loading scenario was not noticed

in the main DOE. That is not to say that there were zero lattices affected by this, but rather that the average values did not appear to be drastically affected by any one value. This image was taken from an initial run of the Strut Deletion DOE. In the most current version of the model, this artificial boundary condition effect is corrected by preventing deletion of edge struts.

Improvements can be made in the displacement boundary condition modeling. Top face keypoints with z dimension keypoint error will be held at the same locations relative to each other throughout the applied load. In reality, any keypoints elevated higher than others would be the first to see a load and would most likely be compressed flat such that the entire lattice upper surface is contacting the platen. This would produce localized yielding at the initial contact point but also may induce overall lattice yielding sooner than expected. A model with fixed-relation top face geometry does not account for that.

4.2.3 Offset Error DOE

The effect of keypoint offset error on load bearing capacity was examined more closely in a separate study. The model was run with 8 different error levels ranging from 0 to 0.8 mm. Five data points were collected for each cell type at each error level, which were averaged, normalized, and plotted in Figure 4.12. Multiple runs were necessary to smooth out a choppy line generated by the random nature of keypoint reassignment. A significant drop in load bearing capability is noted with even a small (0.1 mm) change to keypoint locations. This is most likely due to the changed strut lengths and angles causing stress concentrations in localized spots, when previously the symmetry of the perfect lattices meant there were multiple (usually four) locations sharing that stress.

A distinct difference is noticed amongst the different cell types. Body-Centered

Cubic (BCC) loses the least load capacity, as it drops to only about 70% of its ideal value. The reason it does the best could be because of the symmetry of its mesostructure; though each strut is slightly modified, they carry roughly the same load when neglecting edge effects. The Auxetic cells fare the worst, indicating a strong dependence on its strut arrangement to provide strength. The 90° drops to about 30% of its ideal value.

With increasing offset error, the percentage of ideal levels off. The greatest drop comes between the ideal lattice and 0.1 mm keypoint offset. Values do not stray far from the 0.1 mm force values, even when 8 times the offset is applied. This may be due to the fact that because the error is generated from a uniform random distribution, it is simply creating a structure very similar to that of a stochastic foam.

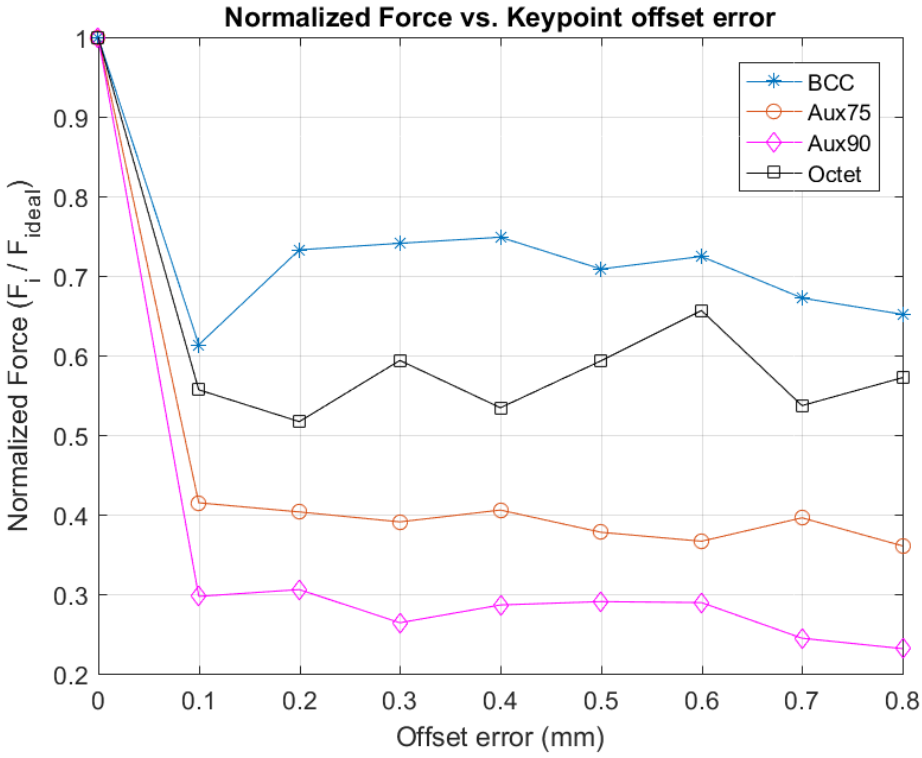

Figure 4.12. Decrease of load bearing capability with increased offset error. Normalized by ideal lattice force. BCC is predicted to lose the least percentage of its original capability, whereas the auxetic cells show significant sensitivity to error.

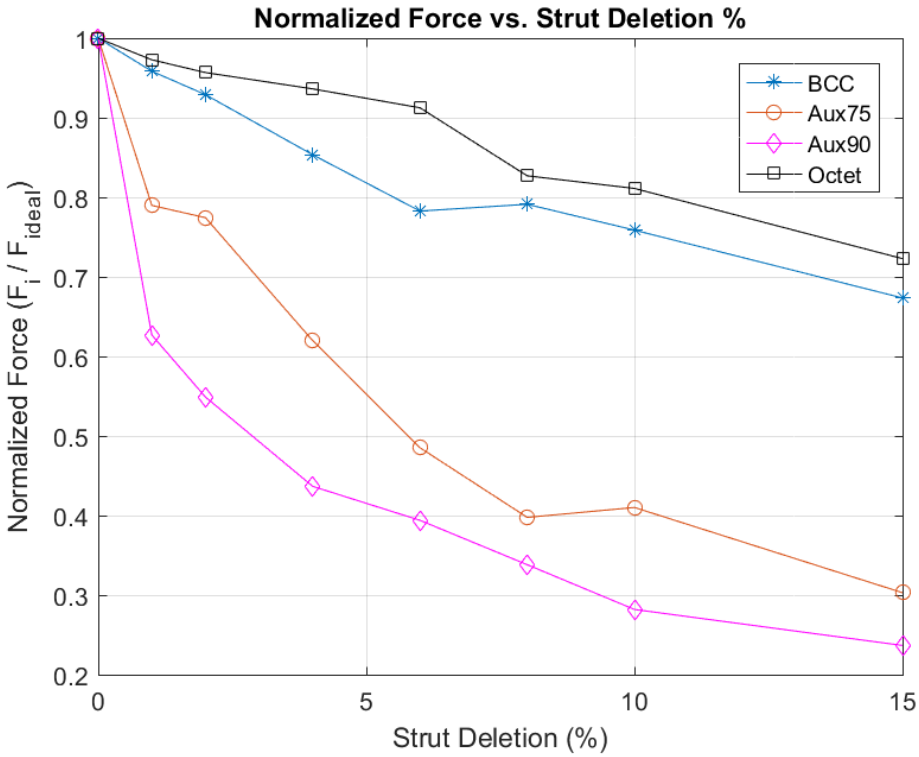

Figure 4.13. Decrease of load bearing capability with increased offset error. Normalized by ideal lattice force. Octet and BCC show better resistance to missing or broken struts than the auxetic cells which appear highly dependent on their ideal geometry.

4.2.4 Strut Deletion DOE

The force at yield results for various percentages of missing struts are plotted in Figure 4.13. Each data point plotted is an average of five runs. Octet and BCC cells show similar responses, approximately a linear decline with percentage removed. These lattices, with 15% of struts removed, dropped to about 70% of their ideal lattice load capacity.

The symmetry of both the BCC and the Octet unit cells minimizes the effects of missing struts. In the BCC cell, every strut is of equal function and capability. No strut is more important than the others like in the Auxetic cell. The octet cell's sheer number of struts handles the missing struts well. They are more directionally dependent than BCC struts, since some are tension bearing and some are compression

bearing, but predictions show that the octet retains the same if not better normalized load bearing capability as the BCC.

The Auxetic cells experienced a steeper drop off in force carrying ability. At 15% of struts removed, the Auxetics dropped to 30% or less of their ideal values. This again indicates geometry dependence, and helps explain why the the main DOE showed the Auxetic 90° lattice to be strongest in ideal configurations, but significantly weaker when imperfections were simulated.

4.3 Experimental Compression Testing Results

PLA plastic lattices were printed using an Ultimaker 2+ Extended 3D printer. The highest load-bearing, ideal, solid strut version of each cell type was selected, printed, and then crushed to find the lattice's overall stiffness and compare force and displacement values to the ANSYS model.

4.3.1 Data and Results

Results from experimental compression tests are listed in Table 4.6. Three runs for each cell type were conducted. Compressed specimens can be seen in Figure 4.14. For each run, the yield values for force, displacement, force per mass, and displacement per mass are presented along experimental mass and stiffness K, found from the force-displacement curves. Mean and standard deviations are given for each value, for each cell type. Table 4.7 compares the average experimental values to the predicted values from the simulation, and Figure 4.19 displays the data in bar charts.

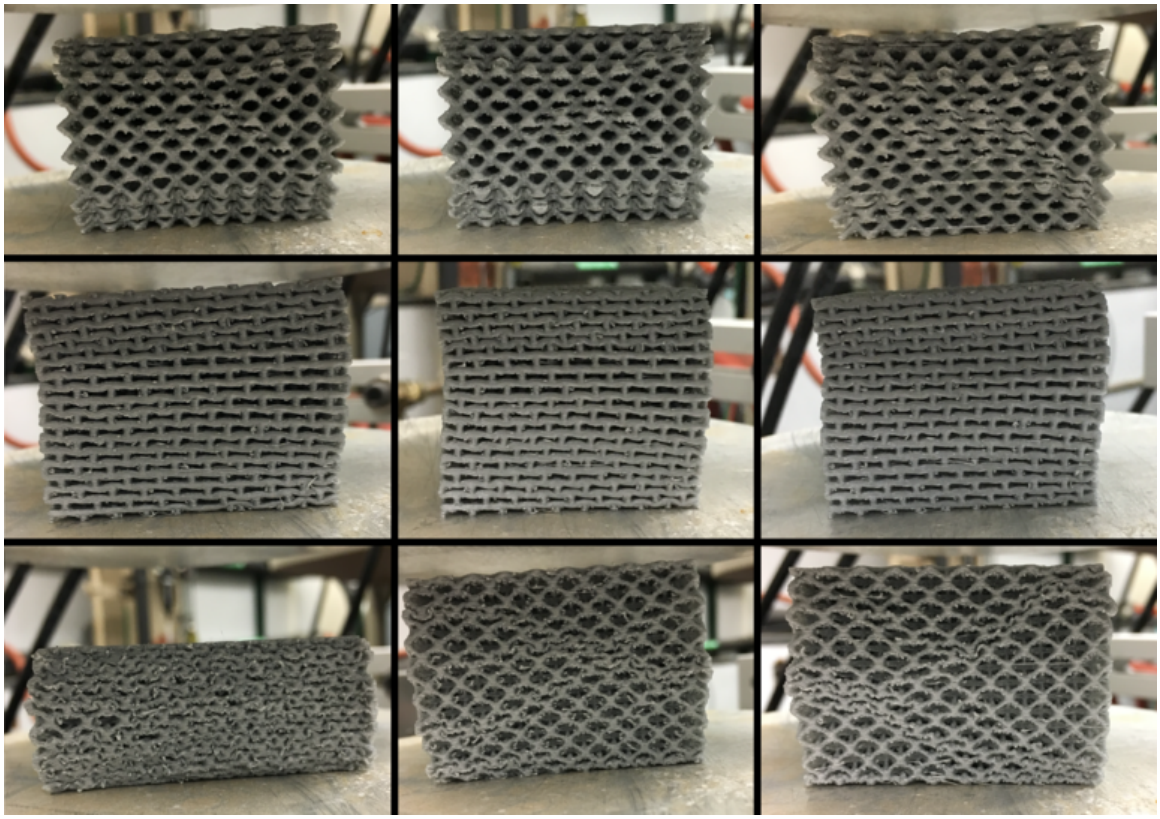

Figure 4.14. Crushed experimental test specimens. Top Row: BCC cell, Runs 1, 2, and 3. Middle Row: Auxetic cell, Runs 1, 2, and 4. Bottom row: Octet cell, Runs 1, 2, and 3. The first Octet run was compressed to densification.

Force vs. Displacement curves for each cell type are seen in Figures 4.15 to 4.17. Experimentally determined yield points are graphed on each curve.

The third run of the Auxetic 90° cell experienced data collection problems, so the force and displacement values are questionable. It was not included in the averaging since its validity could not be determined. An additional Auxetic lattice was printed to take its place.

Table 4.6. Experimental Compression Test Results. 3 specimens per cell type with average and standard deviation.

Run	Yield Disp. (mm)	Yield Force (N)	Mass (g)	Force per mass (N/kg)	Disp. per mass (mm/kg)	Stiffness, K (N/kg):
BCC 1	2.27	12,100	55.6	218,000	40.8	7,410
BCC 2	2.68	11,700	54.2	217,000	49.4	6,250
BCC 3	2.61	12,000	54.8	219,000	47.5	6,530
BCC Avg	**2.52**	**12,000**	**54.9**	**218,000**	**45.9**	**6,730**
BCC Std	0.219	181	0.702	1,260	4.530	604
Octet 1	1.70	13,900	57.7	241,000	29.5	9,530
Octet 2	1.71	14,300	58.5	245,000	29.3	10,200
Octet 3	1.71	14,400	57.9	248,000	29.6	10,200
Octet Avg	**1.71**	**14,200**	**58.0**	**245,000**	**29.4**	**9,980**
Octet Std	0.00644	272	0.416	3,890	0.140	389
Aux90 1	2.31	14,200	66.8	212,000	34.6	6,960
Aux90 2	2.29	14,600	67.3	216,000	34.1	7,150
Aux90 3	~~3.21~~	~~16500~~	66.3	~~249000~~	~~48.4~~	~~9590~~
Aux90 4	2.37	14,500	68.3	212,000	34.7	7,370
Aux90 Avg	**2.32**	**14,400**	**67.5**	**213,000**	**34.4**	**7,160**
Aux90 Std	0.0386	202	0.764	2,550	0.308	207

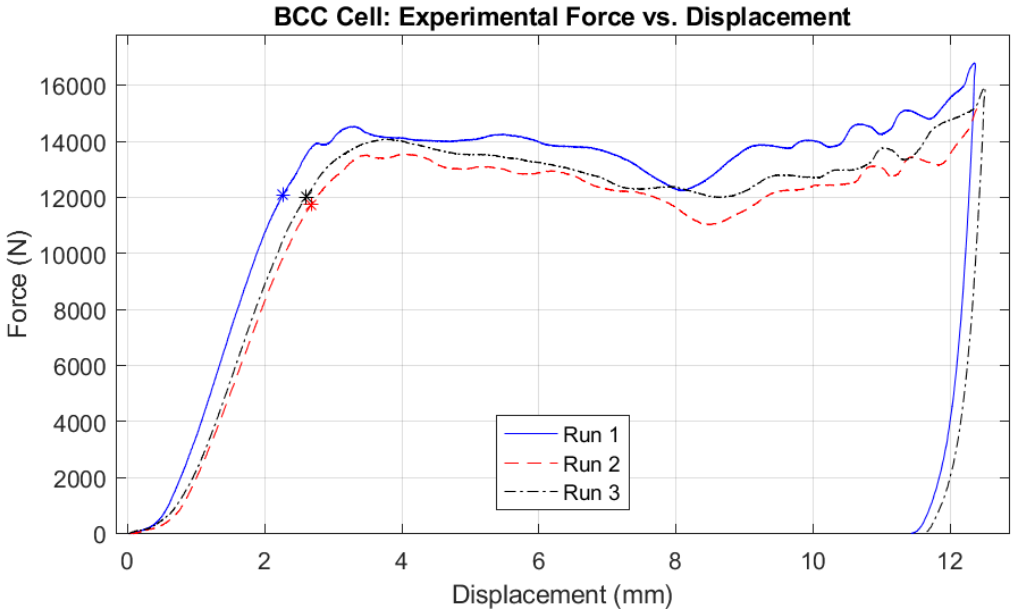

Figure 4.15. Force vs. Displacement for BCC experiments. Yield points are marked with asterisks.

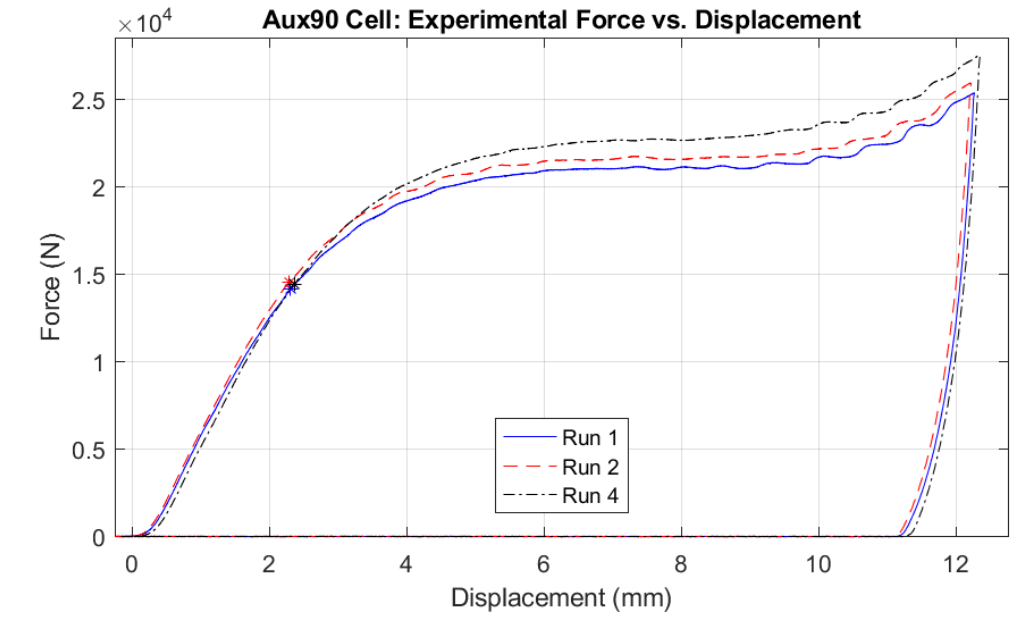

Figure 4.16. Force vs. Displacement for Auxetic experiments. Yield points are marked with asterisks.

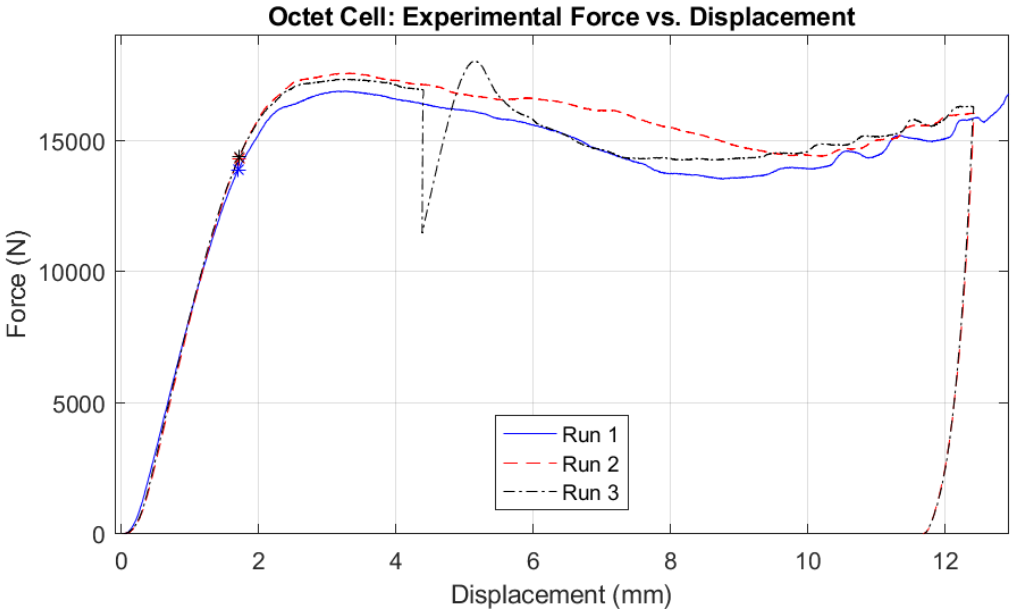

Figure 4.17. Force vs. Displacement for Octet experiments. Yield points are marked with asterisks.

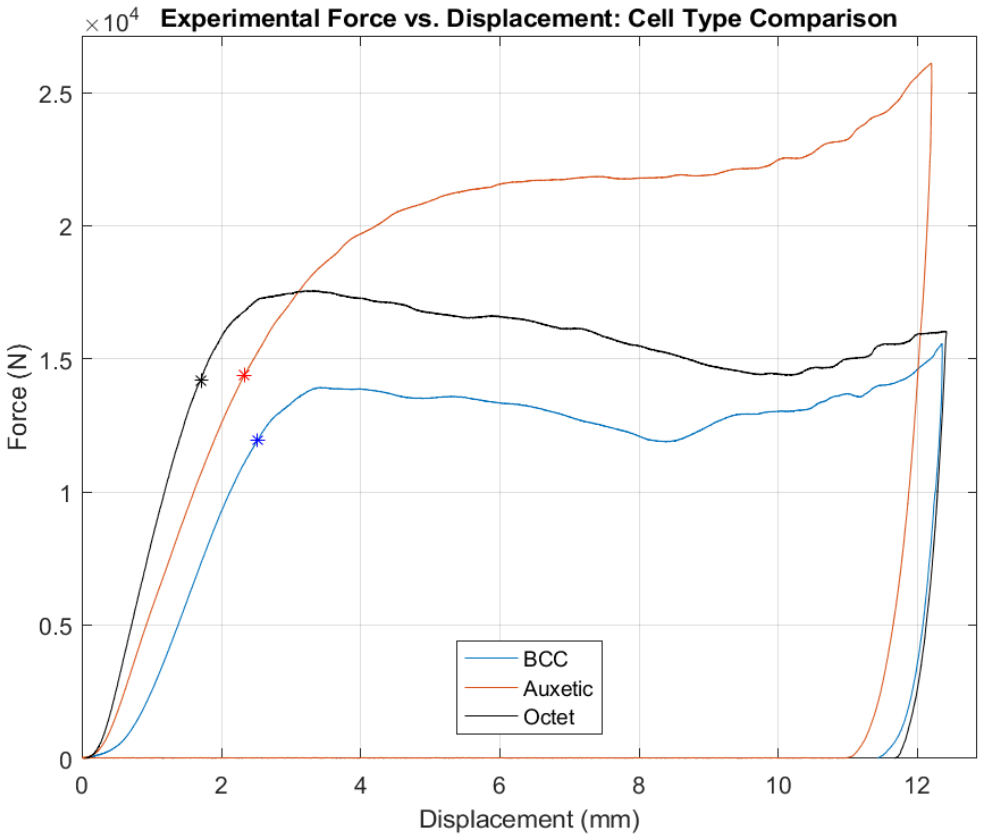

Figure 4.18. Representative Force vs. Displacement curves for all three cell types. Averaged yield points are marked with asterisks.

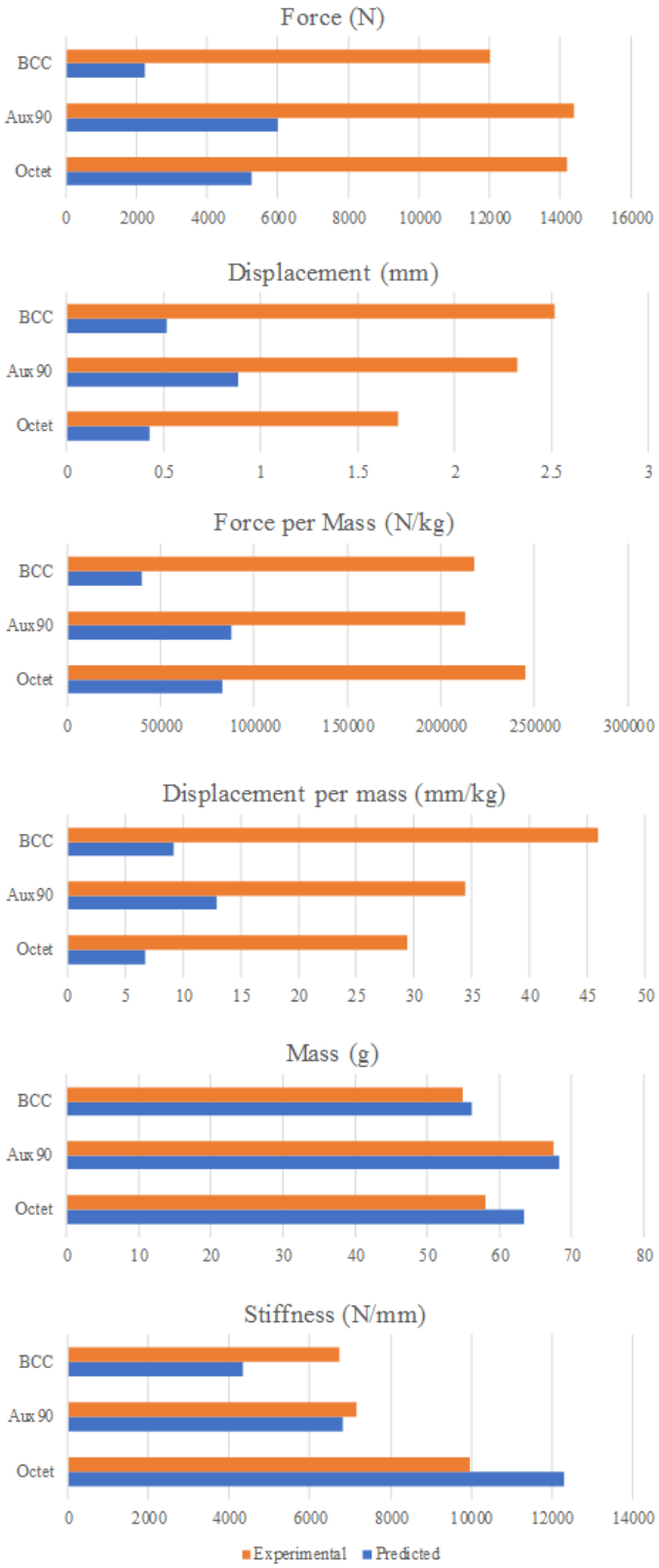

Figure 4.19. Comparison of predicted and experimental results.

Table 4.7. Comparison of predicted and experimental results. Predicted values are from ANSYS with the exception of mass; the mass used for these numbers was calculated using the volume generated by nTopology.

	Stiffness, K (N/mm)	Yield Disp (mm)	Yield Force (N)	Mass (g)	Force per mass (N/kg)	Disp per mass (mm/kg)
BCC Predicted	4,335	0.516	2,235	56.2	39,753	9.17
BCC Experimental	6,731	2.52	12,000	54.87	218,000	45.90
% Error	**-35.6%**	**-79.5%**	**-81.4%**	**2.5%**	**-81.8%**	**-80.0%**
Aux90 Predicted	6,805	0.883	6,011	68.2	88,099	12.95
Aux90 Experimental	7,160	2.32	14,400	67.47	213,000	34.40
% Error	**-5.0%**	**-62.0%**	**-58.3%**	**1.1%**	**-58.6%**	**-62.4%**
Octet Predicted	12,296	0.427	5,253	63.4	82,870	6.74
Octet Experimental	9,978	1.71	14,200	58.03	245,000	29.40
% Error	**23.2%**	**-75.0%**	**-63.0%**	**9.2%**	**-66.2%**	**-77.1%**

4.3.2 Discussion

From the experiments, the octet proves to be the stiffest lattice, while the BCC is the least stiff. The Auxetic cell narrowly beats the octet for highest load at yield, which is similar to predictions from the model. The BCC displaces the furthest before permanent deformation occurs, and also has the highest displacement per mass. Figure 4.18 plots a characteristic average curve of each cell to compare the responses. Average yield points are plotted as asterisks.

The experimental runs were generally in good agreement with each other. Standard deviations were approximately two orders of magnitude smaller than the experimental values. The most apparent difference is between the first BCC test specimen and the other two. There was a 0.3 mm difference in displacement values, where the other two cells had three values that were less than 0.1 mm apart. One explanation for the difference between BCC 1 values and the others was the build process. Specimen BCC 1 was built alone whereas specimens BCC 2 and BCC 3 were simultaneously built next to each other. This created slightly different thermal environments. Each

layer of the simultaneously built lattices received double the cooling period as did the layers of BCC 1. This extra time occurred while the extruder was building the other lattice.

The force displacement curves match the expected trends for the Auxetic lattices. The Auxetic shows yield followed by a long, flat plateau stress region representative of a bending-dominated lattice. The BCC and Octet graphs show similar responses at different magnitudes. The octet shows stretch-dominated characteristics of an initial yield peak followed by a gradual drop in stress. Post-yield softening for a stretch-dominated lattice is expected as struts begin to yield, however the drop off is not immediately discernible as a different response when compared to the BCC plots. The BCC graphs show all runs hover between approximately 12-14 kN after yield, but also show an approximate 2 kN dip at around 8 mm of displacement.

Examination of Octet cell deformation shows a buckling failure mode of external struts. Nodal regions collapse downward into the diamond shaped cavities on the side, twisting the 45° struts supporting them into sharp 's' shapes. Buckling of struts could occur with large displacements or imperfect geometry. Often it occurs in beams with low slenderness ratios, which is defined as the strut diameter to strut length ratio. Examination of the undeformed external surface of an Octet cell reveals varying thickness of struts. Varying strut thickness creates localized weak points where the diameter is smallest. Struts with sufficiently small effective diameters can be expected to respond the same as struts with small slenderness ratios and buckle. These imperfect struts give way under stress and form yield planes.

The fact that the nodal regions are thick compared to the strut diameter promotes buckling. The nodal regions have greater cross sectional area and therefore spread the load better than the thinner, weaker strut sections.

This imperfect geometry from the build process is credited with the cause of buck-

ling and the response seen in the octet's force-displacement curves. Failure by buckling scales E_{rel} with ρ_{rel}^2, rather than ρ_{rel}, which explains why the Octet demonstrates similar force-displacement curves and E_{rel}/ρ_{rel} relationship as the BCC cell. Yield numbers indicate that the octet cell is slightly stronger per mass: BCC maximum force is 85% that of the Octet but is 95% of the mass. However, differences are not by a factor of ρ_{rel} as one would expect based on the scaling laws for a stretch-dominated structure.

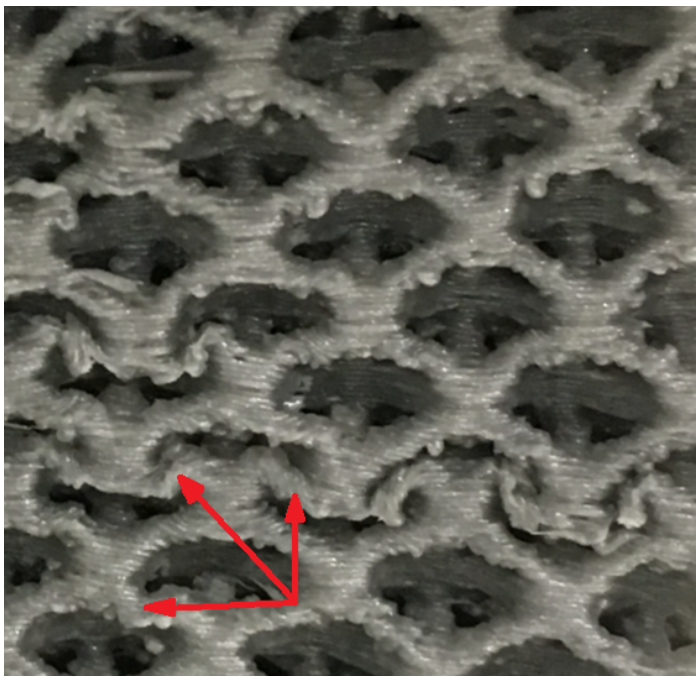

Figure 4.20. Buckling of external Octet struts and imperfect strut geometry.

The Auxetic cell shows a smooth, bending-dominated response on its force-displacement curve. It had the highest yield and plateau force values of all three cells. It very clearly was the best cell for energy absorption over the 12.5 mm of displacement cells were subjected to. The compressed shape was extremely consistent across all four runs. Each run showed bending of the re-entrant struts expected of this cell type. Upper and lower layers tended to deform first as layer collapse trended inward. The Auxetic behavior was negligible for the 90° re-entrant strut; the cell width neither increased

(as the others did) nor decreased, demonstrating a Poisson's ratio of approximately zero. Lateral displacement was evident in each cell where the entire structure bowed to the right from the video camera's view. This response could have stemmed from either build imperfections or slightly uneven pressure from the boundary conditions if the platens were not exactly parallel. Either way, this is a transition between bending of the horizontal struts to buckling of the vertical struts and again shows sensitivity of the Auxetic lattice to imperfection.

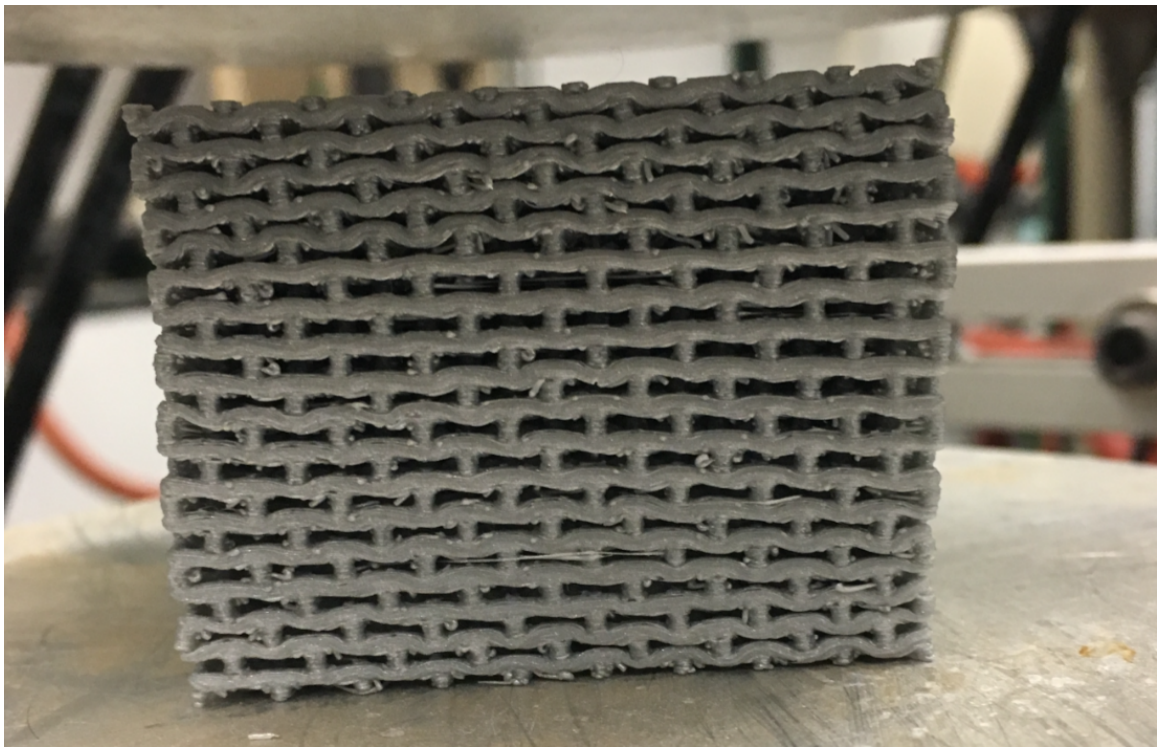

Figure 4.21. Deformed Auxetic cell.

The model significantly underpredicts the performance of each lattice, as seen in Table 4.7 and graphically in Figure 4.19. The closest force prediction was the Auxetic cell force value, 58.3% from the experimental value. Ushijima et al. [19] noticed a similar trend for BCC lattices with strut diameter to cell size ratios of less than 0.1. The printed BCC, Auxetic, and Octet lattices had d/c_s values of 0.324, 0.288, and 0.212, respectively, which are well above the noted threshold. As it is, the model is

not well suited for accurate predictions of lattices with higher levels of d/c_s.

The inaccuracy can be explained by the lack of thickness of the beam elements. The physical specimens have a distinct thickness at keypoint regions that applies constraints to the strut not accounted for by beam elements. These constraints effectively decrease the length of each strut and change based on angle of intersection. The model calculates the stiffness using the longer keypoint-to-keypoint length of the strut, rather than the shorter "effective" length L_{eff} seen in Figure 4.22. Under both axial and bending loads, shorter cylinders are inherently stiffer and deflect less than longer cylinders.

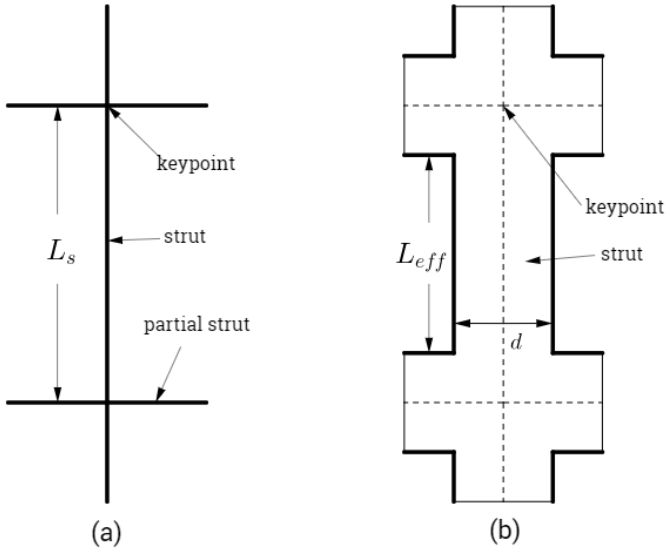

Figure 4.22. (a) Strut length L_s used by the model and (b) Effective strut length L_{eff} seen in physical specimens. This difference can explain differences in predicted and experimental results for higher d/c_s ratio lattices.

The additional strength from the shorter effective strut length is evident when comparing the predicted and experimental values. Modeling the struts to account for the effective length, perhaps with larger diameters near the keypoints, is a recommended improvement to the model and left for future work. The next step in the current model's characterization would be to print experimental specimens with low relative densities/low strut diameter to cell size (d/c_s) ratios. Printing d/c_s ratios

this low may be challenging on an Fused Deposition Modeling (FDM) printer, but would be a perfect application for a Selective Laser Melting (SLM) printer.

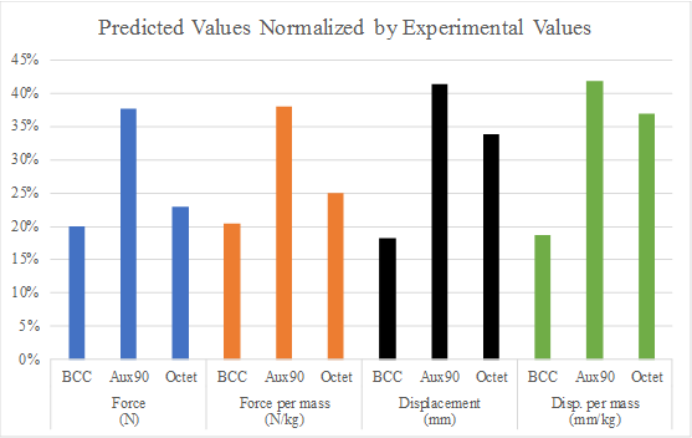

Figure 4.23. Predicted results normalized by Experimental Results.

Figure 4.23 shows the predicted values normalized by the experimental values for the four main categories (displacement, force, displacement per mass, and force per mass at yield). A trend displayed by this graph is that the Auxetic cell was the most accurate while the BCC cell was least accurate in all four categories. This trend indicates differences in the geometries themselves.

A closer look was taken at various methods of mass prediction. The experimental masses of the lattices varied from a value that should have been common to all cells. Theoretically, a 50% dense lattice would be expected to have a mass half that of a solid block of the same overall dimensions. Using the published density of the Ultimaker Polylactic Acid (PLA), each lattice should have a mass of 77.5 g. Various methods of mass calculation are shown in Table 4.8.

The model and ANSYS predicted masses were calculated by very similar methods, summing the volumes of the cylinders. MATLAB was used to independently calculate the volumes, and numbers are nearly identical. This approach is expected to provide an overestimate of mass due to the dual inclusion of overlapped volumes. The experimental masses all came in under the theoretical mass, but matched up

decently with the values calculated with nTopology volume numbers. nTopology calculates the volume enclosed by the triangular surfaces of the .STL file. It also gives the exact dimensions of the bounding box. Because these numbers closely match the experimental masses, a conclusion can be drawn that mass deviation from theoretical is primarily a result of the way the .STL geometry is defined by the nTopology software. Build imperfections are a secondary factor that affect the mass, as small strings and beads of PLA can be seen protruding from struts on all of the lattices.

Table 4.8. Masses calculated by various methods.

(all masses in grams)	BCC	Aux90	Octet
Experiments:	54.9	67.5	58.0
Model predicted:	88.5	107.4	98.2
ANSYS used:	88.5	107.4	98.0
nTopology volume based:	56.2	68.2	63.4
Theoretical Mass, 50% dens, $(50\ \text{mm})^3$ block:	77.5		

Relative values for elastic modulus and density are shown in Table 4.9 and plotted in Figure 4.24. This plot illustrates the $E_{rel} = \rho_{rel}^2$ relationship for bending-dominated structures and the $E_{rel} = \rho_{rel}$ relationship for stretch-dominated ones. All three experimental values are clustered near the upper end of the foams region and slightly below the ideal bending-dominated line. The BCC and Auxetic cells might be expected to end up in this location, but the octet cell shows what is closer to a bending response than an ideal stretching response. Again, this is believed to be due to the fact buckling was noticed in the octet lattices. Under ideal circumstances, the octet would be expected to have a relative elastic modulus value approximately $(1/\rho_{rel})$ times larger than the BCC cell. The predicted values again are under-predictions. Differences between the experimental relative moduli and ideal moduli for their given experimental densities are listed in Table 4.10.

Table 4.9. Mean Experimental values for Relative Elastic Modulus and Relative Density by cell type.

	Relative Elastic Modulus	Relative Density
BCC Avg	4.54E-02	0.315
BCC Std	4.07E-03	0.00403
Aux90 Avg	6.73E-02	0.410
Aux90 Std	2.62E-03	0.00464
Octet Avg	4.92E-02	0.333
Octet Std	1.42E-03	0.00239

Table 4.10. Difference from ideal modulus-density lines for given experimental density.

	Value	Percent
BCC	-0.054	-17.0%
Aux90	-0.101	-24.6%
Octet	-0.284	-85.2%

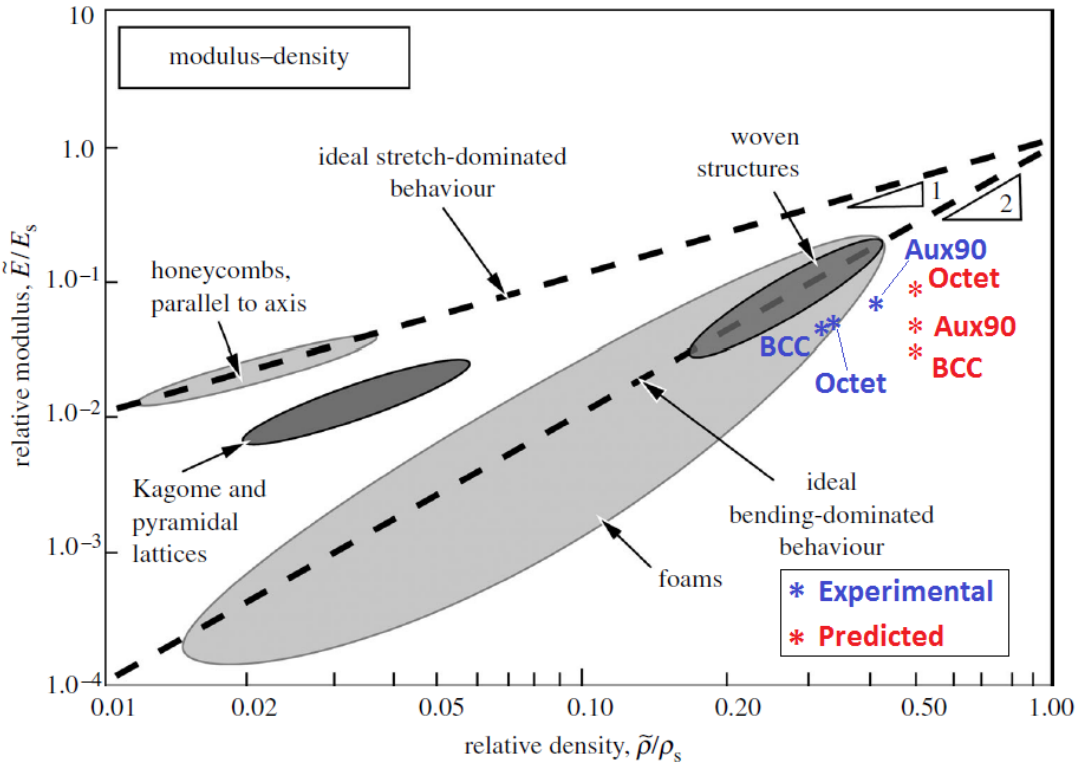

Figure 4.24. Relative elastic modulus vs. relative density plot showing various cellular materials, ideal bending and stretching-dominated behavior, and both FEA and experimental lattice results. Original plot from Ashby [1].

4.4 Summary

This chapter discussed the results from several studies and experimental results. The model underestimated the force and displacement capabilities of each lattice before yield because the strut-to-cell size ratio was too large. Further tests are required to further validate the model. While not accurate for all lattice designs, predictions match expected trends and can be used for trend analysis. Some key takeaways are that lattice strength has a strong dependence on relative density and cell type, and that Auxetic are more sensitive than the other cell types to imperfections.

V. Conclusions and Recommendations

5.1 Summary of Work

This research analyzed additively manufactured lattice structures through use of a novel Finite Element Analysis model and experimental compression testing of several lattices different unit cell geometries.

The modeling tool was talked about in depth as to its features, function, and rationale behind them. The model can be used to generate custom aggregate lattices for analysis and 3D printing. A multitude of lattice geometry and modeling parameters can be easily adjusted by the user to examine their effects on the load bearing capacity and compliance of the aggregate lattice. The model can perform full factorial design of experiments studies to analyze a large combination of variables and compare their impacts.

Results of several FEA studies were presented. First, the re-entrant strut angle of the auxetic cell was studied. The FE models predicted that 90° strut angles delivered the best load bearing and displacement before yield capabilities among angles between 55° and 90°. The primary study examined the effect of several vital geometric parameters on lattice strength and stiffness. Relative density was found to be the most critical variable in determining the strength of the lattice for a given cell type. Octet and Aux90 cell types were predicted as the strongest in the study. The auxetic cell's ideal 90° configuration was predicted to be the strongest of the three cell types, beating out the octet cell which has been studied and found to be a great strength-per-weight lattice suitable for structural applications. Hollow struts also showed desirable strength characteristics as compared to solid struts of the same cross sectional area.

Two other studies examined the effect of damage and imperfection built into

the lattices by the additive manufacturing process. A keypoint offset error study examined random perturbations to strut connection locations (defined by keypoints) on the force load and displacement at yield. Similarly, a strut deletion study removed small percentages of struts from the aggregate lattice and examined the drop in load capability. BCC and octet cells are predicted to exhibit best handling of imperfections in these two studies. This characteristic makes these unit cell types applicable to fabrication methods or scenarios where damage may occur.

Finally, three of the strongest lattices from the main design of experiments study were printed via Fused Deposition Modeling (FDM) and experimentally compression tested. Confidence in the results was achieved by crushing three of each lattice type. Comparison to the model-predicted values showed that the model significantly underestimates the strength of the printed lattices due to the geometric characteristics of the printed lattices. It is theorized that the additional strength is from the strut thickness, which creates an effectively shorter length on the printed geometry than was used for model calculations. With smaller strut diameters, the model is expected to produce more accurate results. Though the values are not accurate, the model does predict historical trends correctly such as the increase of load bearing capability with relative density.

5.2 Future Work

There are many paths to take from this point as far as continued research. Comparison of experimental lattices with low strut diameter to cell size ratios to the model would likely show more accurate results. This would be the first recommended course of action. For lattices with small strut diameters, use of the Selective Laser Melting (SLM) manufacturing method would be preferred to achieve such resolution. More accurate and more consistent specimens are expected from the SLM process.

Improvements can be implemented into the current FE model. Modeling the change in effective strut length for thicker struts should show improvements in accuracy. For faster computation time, symmetry can be included in the Finite Element Model (FEM). The addition of a platen to the printed lattice designs might provide more accurate results and limit warping of the lattices due to thermal effects. It could also make boundary conditions easier to apply (as a single pressure load, rather than many individual force loads at the top face keypoints). Tension, shear, and torsion boundary conditions would be progressive steps in analysis of these lattice structure geometries. New unit cell geometries could be added to compare with the current three.

A variation of the number of unit cells in the cube while maintaining a constant density would be an interesting analysis. Experimental results could show whether cell size has an effect on the properties of the lattice. Imperfections from the build process would be expected to have significant effect on the lattices with larger number of unit cells, since they would have smaller diameter struts to maintain the same density.

Hollow lattices could be studied more in depth. A process for successful production of hollow metal lattices would be useful. A laser powder bed fusion technique would have limitations since the build process would leave powder trapped internally. Additional strength provided by the increased second moment of area for hollow struts may make this worthwhile.

Characterization of the build angle's effect on the material properties would be beneficial. As mentioned in Chapter 2, three studies of build angle on anisotropy yielded three different results. Simple tensile and compression specimens could be built at various angles from the horizontal, and tested to characterize the anisotropy of a given printer. This data could be used with the feature built into the model for varying elastic modulus.

5.3 Conclusion

With the expanding field of AM and the ever-present desire to minimize weight, lattice structures are bound to become more prevalent in new designs. Understanding the behavior of cellular structures is key to implementation of lattice structures. The tool presented here is a helpful accessory to quickly designing, analyzing, and printing lattices for compressively loaded components.

Bibliography

[1] M. Ashby, "The properties of foams and lattices," *Philosophical Transactions of the Royal Society*, vol. 364, pp. 15–30, November 2005.

[2] L. Yang *et al.*, "Mechanical properties of 3d re-entrant honeycomb auxetic structures realized by additive manufacturing," *International Journal of Solids and Structures*, vol. 69-70, pp. 475–490, 2015.

[3] Ultimaker. (2016) Technical data sheet: Pla. [Online]. Available: https://s3-eu-west-1.amazonaws.com/prod.ultimaker.com/download/materials/Ultimaker-PLA-(TDS).pdf

[4] M. Rashed *et al.*, "Metallic microlattice materials: A current state of the art on manufacturing, mechanical properties and applications," *Materials and Design*, vol. 95, pp. 518–533, 2016.

[5] A. G. Bell, "The tetrahedral principle in kite structure," *National Geographic Magazine*, vol. 14, No.6, pp. 219–251, June 1903.

[6] A. Schoen, "Infinite periodic minimal surfaces without self-intersections," NASA Technical Note TN D-5541, 1970.

[7] M. K. Thompson *et al.*, "Design for additive manufacturing: Trends, opportunities, considerations, and constraints," *CIRP Annals - Manufacturing Technology*, vol. 65, p. 737760, 2016.

[8] L. Dong *et al.*, "Mechanical response of ti-6al-4v octet-truss lattice structures," *International Journal of Solids and Structures*, vol. 60-61, pp. 107–124, January 2015.

[9] S. Tsopanos *et al.*, "The influence of processing parameters on the mechanical properties of selectively laser melted stainless steel microlattice structures," *Journal of Manufacturing Science and Engineering-Transactions of the ASME*, vol. 132, no. 4, p. 12, 2010.

[10] X. Ren *et al.*, "Experiments and parametric studies on 3d metallic auxetic metamaterials with tuneable mechanical properties," *Smart Materials and Structures*, vol. 24, pp. 1–15, 2015.

[11] N. Novak *et al.*, "Auxetic cellular materials - a review," *Journal of Mechanical Engineering*, vol. 62, no. 9, pp. 485–493, 2016.

[12] R. Critchley *et al.*, "A review of the manufacture, mechanical properties and potential applications of auxetic foams," *Advanced Engineering Materials*, vol. 15, no. 10, 2013.

[13] V. Deshpande *et al.*, "Effective properties of the octet-truss lattice material," *Journal of the Mechanics and Physics of Solids*, vol. 49, pp. 1747–1769, January 2001.

[14] J. Chu *et al.*, "A comparison of synthesis methods for cellular structures with application to additive manufacturing," 2008.

[15] W. Gao *et al.*, "The status, challenges, and future of additive manufacturing in engineering," *Computer-Aided Design*, vol. 69, pp. 65–89, 2015.

[16] T. Grimm, *User's Guide to Rapid Prototyping*. Society of Manufacturing Engineers, 2004. [Online]. Available: https://books.google.com/books?id=o2B7OmABPNUC&pg=PA55&lpg=PA55&f=false#v=onepage&q&f=false

[17] H. N. Wadley *et al.*, "Fabrication and structural performance of periodic cellular sandwich structures," *Composites Science and Technology*, vol. 63, pp. 2331–2343, 2003.

[18] D. T. Queheillalt and H. N. Wadley, "Cellular metal lattices with hollow trusses," *Acta Materialia*, vol. 53, pp. 303–313, 2004.

[19] K. Ushijima *et al.*, "An investigation into the compressive properties of stainless steel micro-lattice structures," *Journal of Sandwich Structures and Materials*, vol. 13, no. 3, p. 303329, 2010.

[20] E. Andrews *et al.*, "Size effects in ductile cellular solids. part ii: experimental results," *International Journal of Mechanical Sciences*, vol. 43, pp. 701–713, 2001.

[21] R. S. Lakes, "Design considerations for materials with negative poisson's ratios," *Transactions of the ASME*, vol. 115, pp. 696–700, 1993.

[22] D. Tomus *et al.*, "Influence of post heat treatments on anisotropy of mechanical behaviour and microstructure of hastelloy-x parts produced by selective laser melting," *Materials Science and Engineering A*, vol. 667, pp. 42–53, April 2016.

[23] K. Kunze *et al.*, "Texture, anisotropy in microstructure and mechanical properties of in738lc alloy processed by selective laser melting (slm)," *MAterials Science and Engineering A*, vol. 620, pp. 213–222, 2015.

[24] A. Deev *et al.*, "Anisotropy of mechanical properties and its correlation with the structure of the stainless steel 316l produced by the slm method," *Physics Procedia*, vol. 83, pp. 789–796, 2016.

[25] H. Meier and C. Haberland, "Experimental studies on selective laser melting of metallic parts," *Materialwissenschaft und Werkstofftechnik*, vol. 39, pp. 665–670, 2008.

[26] W. Shifeng *et al.*, "Effect of molten pool boundaries on the mechanical properties of selective laser melting parts," *Journal of Materials Processing Technology*, vol. 214, pp. 2660–2667, 2014.

[27] K. Guan *et al.*, "Effects of processing parameters on tensile properties of selective laser melted 304 stainless steel," *Materials and Design*, vol. 50, pp. 581–586, 2013.

[28] R. D. Cook *et al.*, *Concepts and Applications of Finite Element Analysis*, 4th ed. Hoboken, NJ: John Wiley and Sons, Inc., 2002.

[29] *ANSYS Mechanical APDL Element Reference*, ANSYS, Inc., 2016.

[30] W. F. Riley *et al.*, *Statics and Mechanics of Materials: An Integrated Approach*, 2nd ed. John Wiley and Sons, Inc., 2002.

[31] E. W. Weisstein. (2016) Steinmetz solid. [Online]. Available: http://mathworld.wolfram.com/SteinmetzSolid.html

REPORT DOCUMENTATION PAGE

Form Approved
OMB No. 0704–0188

1. REPORT DATE *(DD–MM–YYYY)*	2. REPORT TYPE	3. DATES COVERED *(From — To)*
23 March 2017	Master's Thesis	1 April 2016 — 23 March 2017

4. TITLE AND SUBTITLE

ANALYSIS OF ADDITIVELY MANUFACTURED LATTICE STRUCTURES USING FINITE ELEMENT METHODS

5a. CONTRACT NUMBER

5b. GRANT NUMBER

5c. PROGRAM ELEMENT NUMBER

6. AUTHOR(S)

Box, Christopher, A., Capt

5d. PROJECT NUMBER

JON 17Y372

5e. TASK NUMBER

5f. WORK UNIT NUMBER

7. PERFORMING ORGANIZATION NAME(S) AND ADDRESS(ES)

Air Force Institute of Technology
Graduate School of Engineering and Management (AFIT/EN)
2950 Hobson Way
WPAFB OH 45433-7765

8. PERFORMING ORGANIZATION REPORT NUMBER

AFIT-ENY-MS-17-M-245

9. SPONSORING / MONITORING AGENCY NAME(S) AND ADDRESS(ES)

AFRL/RWMW
Att: Dr. Philip Flater
2306 Perimeter Road, Bldg 1190
Eglin AFB, FL 32542
Email: philip.flater@us.af.mil

10. SPONSOR/MONITOR'S ACRONYM(S)

AFRL/RW

11. SPONSOR/MONITOR'S REPORT NUMBER(S)

12. DISTRIBUTION / AVAILABILITY STATEMENT

DISTRIBUTION STATEMENT A:
APPROVED FOR PUBLIC RELEASE; DISTRIBUTION UNLIMITED.

13. SUPPLEMENTARY NOTES

14. ABSTRACT

Additive Manufacturing (AM) processes are well known for their ability to fabricate parts with complex geometries. Lattice structures leverage this ability to create parts with high strength-to-weight ratio and other desirable structural qualities. This research presents a parameterized modeling tool using common Finite Element Analysis (FEA) and scripting software with which aggregated lattice structures can be analyzed, given different geometric properties and loading conditions. A full factorial Design of Experiments is run to explore the effects of various parameters on the strength of lattice structures. Experimental compressive strength results from three FDM-produced PLA lattices are discussed and compared to predictions from the Finite Element simulations.

15. SUBJECT TERMS

Lattice Structures, Additive Manufacturing, Finite Element Analysis, PLA plastic printing

16. SECURITY CLASSIFICATION OF:			17. LIMITATION OF ABSTRACT	18. NUMBER OF PAGES	19a. NAME OF RESPONSIBLE PERSON
a. REPORT	b. ABSTRACT	c. THIS PAGE			Maj Ryan P. O'Hara, Ph.D., AFIT/ENY
U	U	U	UU	117	19b. TELEPHONE NUMBER *(include area code)* (937) 255-3636, x4542; ryan.ohara@afit.edu